Article

Molecular Cell

Non-canonical mTORC2 Signaling Regulates Brown Adipocyte Lipid Catabolism through SIRT6-FoxO1

Graphical Abstract

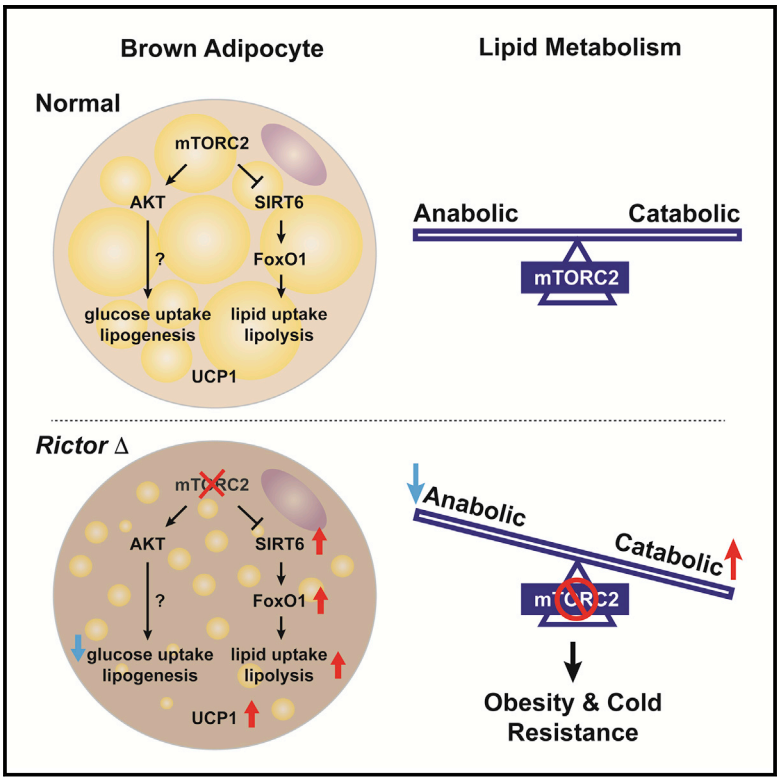

Highlights

- Inhibiting brown adipocyte mTORC2 protects against obesity at thermoneutrality
- mTORC2 suppresses lipolysis and UCP1 expression
- Inhibiting mTORC2 triggers FoxO1 deacetylation by SIRT6
- FoxO1 drives lipid catabolism upon mTORC2 loss

Authors

Su Myung Jung, Chien-Min Hung, Samuel R. Hildebrand, ..., Raul Mostoslavsky, Christian M. Metallo, David A. Guertin

Correspondence

david.guertin@umassmed.edu

In Brief

Jung et al. identify an mTORC2-SIRT6-FoxO1 pathway in brown adipocyte that suppresses lipid catabolism and UCP1 expression independently of mTORC2's role in promoting *de novo* lipogenesis. Mice lacking brown fat mTORC2 are protected against diet-induced obesity, uncovering a new mechanism in brown fat that regulates systemic metabolic homeostasis.

Jung et al., 2019, Molecular Cell *75*, 807–822
August 22, 2019
https://doi.org/10.1016/j.molcel.2019.07.023

CellPress

Molecular Cell
Article

Non-canonical mTORC2 Signaling Regulates Brown Adipocyte Lipid Catabolism through SIRT6-FoxO1

Su Myung Jung,[1,8] Chien-Min Hung,[1,8] Samuel R. Hildebrand,[1] Joan Sanchez-Gurmaches,[1,3,4] Barbara Martinez-Pastor,[6] Jivani M. Gengatharan,[5] Martina Wallace,[5] Dimpi Mukhopadhyay,[1] Camila Martinez Calejman,[1] Amelia K. Luciano,[1] Wen-Yu Hsiao,[1] Yuefeng Tang,[1] Huawei Li,[1] Danette L. Daniels,[7] Raul Mostoslavsky,[6] Christian M. Metallo,[5] and David A. Guertin[1,2,9,*]

[1]Program in Molecular Medicine, University of Massachusetts Medical School, Worcester, MA 01605, USA
[2]Department of Molecular, Cell and Cancer Biology, University of Massachusetts Medical School, Worcester, MA 01605, USA
[3]Division of Endocrinology, Developmental Biology, Cincinnati Children's Hospital Research Foundation, University of Cincinnati College of Medicine, Cincinnati, OH 45209, USA
[4]Department of Pediatrics, University of Cincinnati College of Medicine, Cincinnati, OH 45209, USA
[5]Department of Bioengineering, University of California, San Diego, La Jolla, CA 92093, USA
[6]The Massachusetts General Hospital Cancer Center, Harvard Medical School, Boston, MA 02114, USA
[7]Promega Corporation, 2800 Woods Hollow Road, Madison, WI 53711, USA
[8]These authors contributed equally
[9]Lead Contact
*Correspondence: david.guertin@umassmed.edu
https://doi.org/10.1016/j.molcel.2019.07.023

SUMMARY

mTORC2 controls glucose and lipid metabolism, but the mechanisms are unclear. Here, we show that conditionally deleting the essential mTORC2 subunit *Rictor* in murine brown adipocytes inhibits *de novo* lipid synthesis, promotes lipid catabolism and thermogenesis, and protects against diet-induced obesity and hepatic steatosis. AKT kinases are the canonical mTORC2 substrates; however, deleting *Rictor* in brown adipocytes appears to drive lipid catabolism by promoting FoxO1 deacetylation independently of AKT, and in a pathway distinct from its positive role in anabolic lipid synthesis. This facilitates FoxO1 nuclear retention, enhances lipid uptake and lipolysis, and potentiates UCP1 expression. We provide evidence that SIRT6 is the FoxO1 deacetylase suppressed by mTORC2 and show an endogenous interaction between SIRT6 and mTORC2 in both mouse and human cells. Our findings suggest a new paradigm of mTORC2 function filling an important gap in our understanding of this more mysterious mTOR complex.

INTRODUCTION

A cell's ability to balance anabolism and catabolism in response to nutrient availability is essential for metabolic fitness. The mTOR kinase, which senses intracellular nutrients through metabolite-sensing pathways and systemic nutrients through growth factor signaling, is critical for this metabolic flexibility (Lee et al., 2017; Saxton and Sabatini, 2017). mTOR's functions are split between two biochemically distinct complexes called mTOR complex 1 (mTORC1) and mTOR complex 2 (mTORC2). mTORC1 contains the essential subunit Raptor and is an amino acid and growth factor-sensing complex that drives macromolecule biosynthesis and suppresses autophagy through well-defined pathways. mTORC2 uniquely contains the essential subunit Rictor and is implicated in glucose and lipid metabolism, but its regulation and mechanisms of action are more mysterious.

The canonical mTORC2 substrate is AKT, which it phosphorylates on a C-terminal hydrophobic motif (HM) site (S473) (Sarbassov et al., 2005). AKT is also phosphorylated by PDK1 on the kinase domain T-loop motif (T308). T-loop phosphorylation is essential for catalytic activity, while HM phosphorylation promotes maximum AKT activity (Manning and Toker, 2017). *In vitro*, knocking down *Rictor* or acutely treating cells with an mTOR kinase inhibitor reduces T-loop phosphorylation (Sarbassov et al., 2005; Thoreen et al., 2009; Peterson et al., 2009; Feldman et al., 2009). However, HM phosphorylation is not essential for T-loop phosphorylation, as genetic models show that they can occur independently *in vivo* (Shiota et al., 2006; Jacinto et al., 2006; Guertin et al., 2006; Lee et al., 2017; Manning and Toker, 2017; Leroux et al., 2018). Moreover, many conditional *Rictor*-knockout models have profound metabolic phenotypes but often with normal or mild effects on AKT substrate phosphorylation (Hung et al., 2014; Lee et al., 2017; Gaubitz et al., 2016). Thus, the exact function of mTORC2 in AKT signaling is unresolved, and whether mTORC2 has AKT-independent functions in metabolism is unclear.

Brown adipose tissue (BAT) is specialized for non-shivering thermogenesis (NST), which is an adaptive response to cold temperature. NST is stimulated by the sympathetic nervous system and characterized by increased glucose uptake and *de novo* lipogenesis (DNL) in addition to increased lipolysis, fatty acid (FA)

uptake, and FA oxidation (Cannon and Nedergaard, 2004; Scheele and Nielsen, 2017; Sanchez-Gurmaches et al., 2018; Mottillo et al., 2014). NST is also triggered by high-fat diet (HFD), termed diet-induced thermogenesis (DIT) to distinguish it from cold-induced thermogenesis (CIT). Both modes of thermogenesis are mediated by uncoupling protein 1 (UCP1), which dissipates chemical energy as heat (Rothwell and Stock, 1979; Cannon and Nedergaard, 2004; Feldmann et al., 2009; von Essen et al., 2017). In mice, NST is low in the absence of thermal or dietary stress. Lowering the environmental temperature below the thermoneutral zone stimulates CIT, while DIT is stimulated when thermoneutral housed mice are fed a HFD (Feldmann et al., 2009; Rowland et al., 2016; von Essen et al., 2017; Fischer et al., 2019). Although CIT helps maintain euthermia, DIT protects against obesity demonstrated by the fact that *Ucp1*−/− mice living at thermoneutrality are prone to obesity (Feldmann et al., 2009; von Essen et al., 2017; Kontani et al., 2005).

In mice, interscapular brown adipocytes originate from Myf5-expressing precursors during development (Seale et al., 2008; Sanchez-Gurmaches and Guertin, 2014; Sanchez-Gurmaches et al., 2016). We previously showed that *Myf5-cre;Rictor* mice have small lipid-depleted interscapular brown adipocytes with enlarged mitochondria and altered lipid metabolism (Hung et al., 2014). Unexpectedly, *Myf5-cre;Rictor* brown adipocytes appear to have normal downstream AKT signaling to many classic substrates. A similar paradox is observed in *Adiponectin-cre;Rictor* mice, which have impaired insulin-stimulated glucose uptake into white adipose tissue (WAT) and systemic insulin resistance despite seemingly normal AKT signaling (Tang et al., 2016). These findings hint at the existence of undefined mTORC2 mechanisms critical for carbohydrate and lipid metabolism.

Acclimating mice to thermoneutrality lowers their basal metabolism to be more human-like, profoundly influencing many phenotypes (Cannon and Nedergaard, 2011; Gordon et al., 2014; Hylander and Repasky, 2016). Interestingly, *Myf5-cre;Rictor* mice living at thermoneutrality are protected from diet-induced obesity (Hung et al., 2014), a finding of clinical interest given efforts to develop anti-obesity therapies targeting thermogenesis (Harms and Seale, 2013; Sidossis and Kajimura, 2015; Scheele and Nielsen, 2017). However, Myf5-Cre expresses in many non-brown adipocyte lineages, including several white adipocytes, muscle, bone, and neuronal cells (Sanchez-Gurmaches et al., 2016), questioning the specificity of this phenotype to brown fat.

Here, we show that inhibiting brown adipocyte mTORC2 cell-autonomously potentiates thermogenesis, which enhances heat production in the cold and protects against obesity at thermoneutrality. Mechanistically, inhibiting BAT mTORC2 drives lipid catabolism in part by activating the FoxO1 transcription factor by driving SIRT6-mediated FoxO1 deacetylation independently of AKT and the related mTORC2 substrate SGK. This branch of mTORC2 signaling appears to be independent of mTORC2's role in promoting DNL. These findings fill an important gap in our understanding of how mTORC2 balances anabolic and catabolic lipid metabolism and expose a new aspect of mTORC2 signaling that may be relevant in diabetes and cancer.

RESULTS

mTORC2 Suppresses UCP1 Expression

Using AKT1-S473 and AKT2-S474 phospho-specific antibodies as reporters, we asked if CIT affects BAT mTORC2 activity. AKT1-S473 phosphorylation (P-AKT1-S473) is comparable between mice living at thermoneutrality (30°C) and mild cold (22°C) but decreases dramatically upon acclimation to severe cold (6°C) (Figure 1A). Consistent with our previous work, AKT2-S474 phosphorylation and total protein increase at 22°C (Sanchez-Gurmaches and Guertin, 2014). However, whereas total AKT2 protein remains elevated in severe cold, P-AKT2-S474 markedly decreases (Figure 1A). The coordinated decrease of P-AKT1-S473 and P-AKT2-S474 in severe cold inversely correlates with UCP1 expression, suggesting that mTORC2 may suppress thermogenesis.

To acutely examine brown adipocyte mTORC2 function *in vitro*, we developed a brown adipocyte *CreER;rictor* model in which 4-hydroxytamoxifen (4-OHT) or vehicle (ethanol) treatment generates *Rictor*-inducible knockout (*Rictor-iKO)* brown adipocytes and their isogenic control, respectively (Figure 1B). *Rictor-iKO* brown adipocytes lack Rictor and AKT-HM phosphorylation (Figure 1C). To mimic β-adrenergic receptor stimulation, cells were treated with the β3 adrenergic receptor agonist CL-316,243 or the adenylyl cyclase activator forskolin. Strikingly, both agonists more potently induce UCP1 mRNA and protein expression in the *Rictor-iKO* brown adipocytes compared with control cells (Figures 1C and 1D). Expression of the brown fat identity genes *Pgc1a* and *Cidea* is also stimulated by *Rictor* loss (Figures 1E and 1F), while *Pparg2* and *Prdm16* are unaffected (Figures 1G and 1H). Similar effects are observed in primary *adiponectin-cre;rictor* brown adipocytes (Figures S1A and S1B), and in *Rictor-iKO* brite or beige adipocytes (Figures S1C and S1D), the latter additionally having increased *Fgf21* and *Pdk4* expression indicative of WAT browning (Figure S1D) (Fisher et al., 2012; Barquissau et al., 2016). These data are consistent with mTORC2 cell-autonomously suppressing thermogenesis.

Conditionally Knocking Out *Rictor* in BAT Improves Cold Tolerance

To examine the physiological role of mTORC2 in BAT, we generated *Ucp1-Cre;Rictor* conditional knockout mice (hereafter $Rictor^{BATKO}$). $Rictor^{BATKO}$ mice living in standard conditions (22°C, chow diet) have 46% less BAT mass compared with controls (Figure 2A) because of smaller lipid droplets (Figure 2B). Liver mass is also reduced by 11%, while the mass of subcutaneous and visceral WAT, skeletal muscle, heart, kidney, spleen, lung, and thymus is normal (Figure 2A). Western blots confirm loss of Rictor, P-AKT-S473, and AKT turn motif (T450) phosphorylation—a growth factor-insensitive mTORC2-dependent phosphorylation site affecting AKT mobility (Facchinetti et al., 2008)—only in BAT but not in WAT (Figures 2C, 2D, S2A, and S2B). Despite *Rictor*-deficient BAT lacking P-AKT-S473, PDK1 still phosphorylates AKT in the T-loop (T308), albeit at slightly lower levels (Figures 2C and S2A). Consistent with our previous work on adipocytes (Tang et al., 2016; Hung et al., 2014), $Rictor^{BATKO}$ mice express 83% less levels of

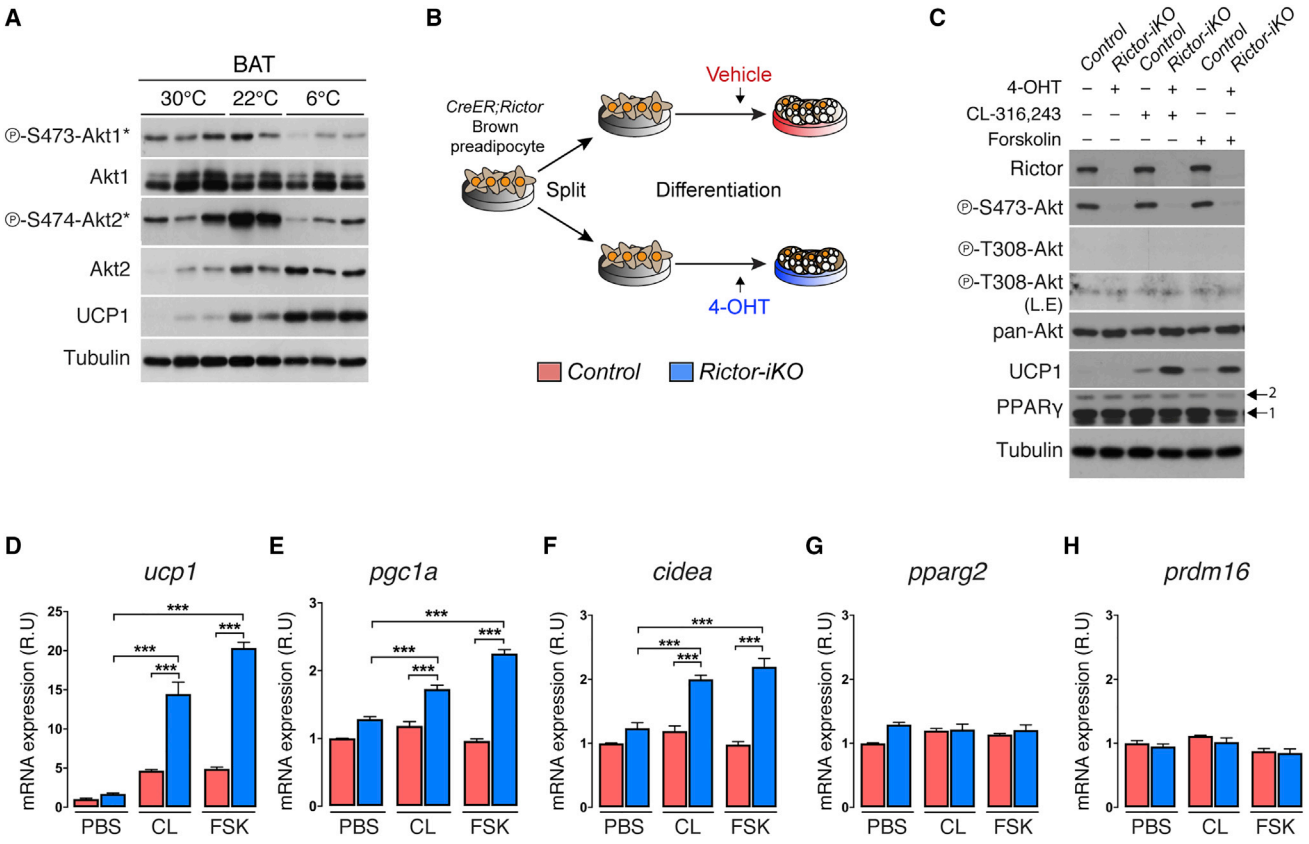

Figure 1. mTORC2 Suppresses UCP1 Expression *In Vitro*

(A) Western blots of the indicated proteins using BAT lysates from wild-type 14-week-old male C57/BL6J mice adapted to thermoneutrality (30°C) for 4 weeks, mild cold (22°C), or severe cold (6°C) for 2 weeks. Mice were fed a standard chow diet *ad libitum*. The asterisk indicates isoform-specific phospho-antibodies for AKT1 or AKT2.

(B) Experimental strategy for inducing *Rictor* deletion in mature brown adipocytes. Vehicle or 4-hydroxytamoxifen (4-OHT) is administered late during differentiation (day 6 of differentiation) to achieve fully differentiated cells acutely deleted for *Rictor* (also see STAR Methods).

(C) Western blot showing CL-316,243 (0.1 μM, 8 h) or forskolin (1 μM, 8 h) stimulated UCP1 expression in *Rictor-iKO* brown adipocytes compared with their isogenic controls. L.E., long exposure. Arrows indicate the PPARγ1 and 2 isoforms.

(D–H) qRT-PCR analysis showing CL-316,243 (CL; 0.1 μM, 8 h) or forskolin (FSK; 1 μM, 8 h) stimulated gene expression in *Rictor-iKO* brown adipocytes compared with their isogenic controls (n = 3); *ucp1* (D), *pgc1a* (E), *cidea* (F), *pparg2* (G), *prdm16* (H). PBS, phosphate buffered saline control. Data are mean ± SEM. Statistical significance was calculated using two-way ANOVA with Tukey's multiple-comparisons test: *p < 0.05, **p < 0.01, and ***p < 0.001 (control versus *Rictor-iKO*, PBS treated versus CL or FSK treated).

Chrebpβ (Figure 2E), which encodes a transcriptional activator of *de novo* lipogenesis (DNL) (Eissing et al., 2013; Herman et al., 2012) and nearly 70%–80% less levels of its target genes *Acly* (78%), *Acc* (70%), *Fasn* (70%), and *Elovl6* (70%) (Figure 2E). This accounts for a dramatic reduction in total ACLY, ACC, and FASN protein (Figure 2C), indicating profound downregulation of the DNL pathway upon mTORC2 loss. Thus, in mice living in standard vivarium conditions, BAT mTORC2 positively regulates BAT size and lipid content.

Rictor^{BATKO} mice have a normal average body temperature of around 38.2°C in standard living conditions (Figure 2F). In response to an acute severe cold challenge (6°C for 7 h), *Rictor*^{BATKO} mice maintain a slightly warmer body temperature (Figure 2F) that correlates with higher BAT heat production determined directly by thermal camera imaging (Figure 2). *Rictor*^{BATKO} mice maintain euthermia for up to 2 weeks at 6°C, which also correlates with higher BAT heat production (Figures 2G and 2H). Consistent with the *in vitro* model (Figure 1C), BAT UCP1 levels are dramatically elevated in *Rictor*^{BATKO} mice (Figure 2C) confirming that mTORC2 also suppresses UCP1 expression *in vivo*. Thus, BAT mTORC2 is dispensable for maintaining euthermia in the cold, and its loss enhances CIT.

Prolonged severe cold (6°C) exposure also stimulates subcutaneous WAT browning. The formation of individual brite or beige adipocytes in WAT can be marked in *ucp1-cre*-expressing mice by incorporating the Cre-activated mTmG reporter (Muzumdar et al., 2007) (Figure S2C). Comparing brite or beige adipocyte formation between *Ucp1-Cre;Rictor;mTmG* mice and their *ucp1-cre;mTmG* controls reveals that the *Rictor*-deficient brite or beige adipocytes are smaller and more multi-locular (Figure S2D). However, the total number of brite or beige adipocytes

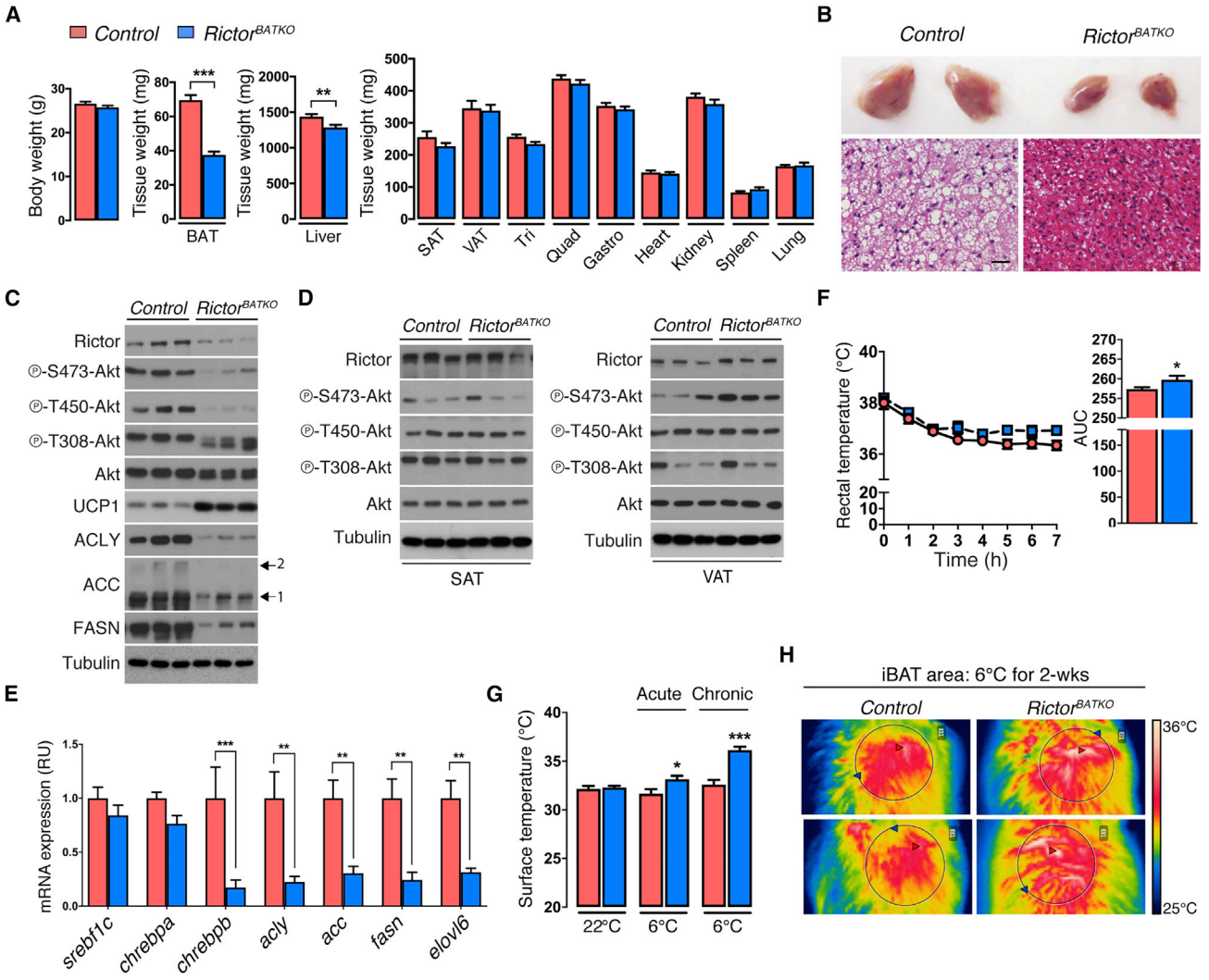

Figure 2. Increased Cold Tolerance and UCP1 Expression in *Rictor*^{BATKO} Mice

(A) Tissue mass data from *Rictor*^{BATKO} mice and controls under standard conditions (22°C, fed *ad libitum* with a standard chow diet, 14-week-old males, n = 11).

(B) Top: representative photograph of the interscapular BAT (iBAT) depots from a *Rictor*^{BATKO} mouse and a littermate control living in standard conditions. Bottom: representative H&E staining images. Scale bar, 100 μm.

(C) Western blots in triplicate using total BAT lysates from *Rictor*^{BATKO} mice and controls living in standard conditions.

(D) Same as (C) except using subcutaneous adipose tissue (SAT) and visceral adipose tissue (VAT) depots.

(E) qRT-PCR analysis using BAT from *Rictor*^{BATKO} mice and controls living in standard conditions (n = 8).

(F) Rectal temperatures during an acute cold challenge (6°C) starting from 22°C (fed *ad libitum* with a standard chow diet, 10-week-old males, n = 9 or 10).

(G) Infrared thermography of the skin surface temperature directly above the iBAT depot from mice acclimated to 6°C for 7 h (acute) or 2 weeks (chronic) (n = 4–8).

(H) Representative images from (G).

Data are mean ± SEM. Statistical significance was calculated using two-tailed unpaired Student's t test (A and F, right), two-way ANOVA with Sidak's multiple-comparisons test (E and G), and two-way repeated-measures ANOVA with Sidak's multiple-comparisons test (F, left): *p < 0.05, **p < 0.01, and ***p < 0.001 (control versus *Rictor*^{BATKO}).

(determined by counting mGFP-positive cells) remains the same (Figure S2E). The *Ucp1-Cre;Rictor* brite or beige adipocytes also express higher levels of *Ucp1*, *Pgc1a* (Figure S2F), and trend toward higher UCP1 protein (Figure S2G). We did not detect a decrease in total Rictor protein in whole SAT lysates from these mice (Figure S2G), but this is perhaps not surprising given the greater heterogeneity of SAT compared with BAT (Roh et al., 2017). Nevertheless, during prolonged severe cold exposure, enhanced WAT browning could also contribute to CIT in *Ucp1-Cre;Rictor* mice.

Rictor^{BATKO} Mice Are Resistant to Diet-Induced Obesity

Next, we acclimated *Rictor*^{BATKO} mice to 30°C and either kept them on standard chow diet (SCD) or switched them to HFD to trigger DIT. Weekly monitoring of body weight reveals no difference between the cohorts on SCD; however, *Rictor*^{BATKO} mice

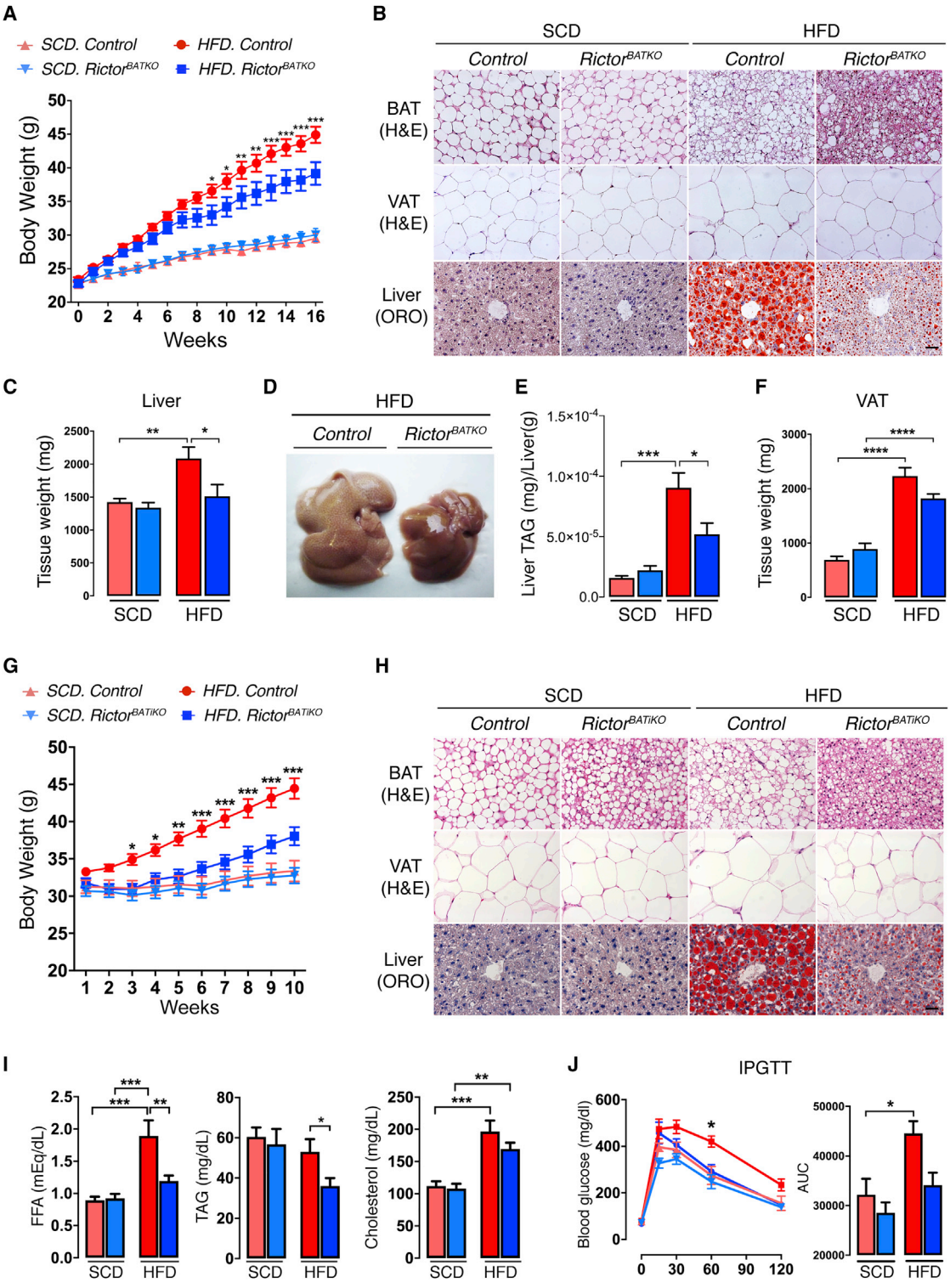

Figure 3. *Rictor*^{BATKO} Mice Are Protected from Diet-Induced Obesity at Thermoneutrality

(A) Growth curves of *Rictor*^{BATKO} mice and controls living at 30°C and eating either standard chow diet (SCD) or HFD; n = 8–12 male mice per group.

(B) Representative H&E (BAT, VAT) and oil red O (liver) staining images from mice in (A). Scale bar, 100 μm.

(C) Average liver mass of mice in (A) (n = 8–12).

(D) Representative photograph of livers from HFD-fed control and *Rictor*^{BATKO} mice in (A).

(E) Corresponding liver TAG quantification for (D) (n = 7).

(legend continued on next page)

on HFD gain less weight (Figure 3A). Living without thermal stress causes whitening of BAT in both the control and *Rictor*^{BATKO} mice on SCD (Figure 3B). In contrast, control mice on HFD have abundant multi-locular adipocytes, indicating DIT (Figure 3B); this is strikingly magnified in HFD-fed *Rictor*^{BATKO} mice, which have BAT size, color, and morphology more akin to cold-stressed mice (Figures 3B, S3A, and S3B). In control mice eating HFD, liver mass increases by 45% over SCD-fed controls (Figure 3C). Liver mass is unchanged in the SCD-fed *Rictor*^{BATKO} mice compared with controls (Figure 2A) suggesting that *Rictor*-deficient BAT is inert in the absence of thermal or dietary stress. In contrast, *Rictor*^{BATKO} mice on HFD are resistant to hepatomegaly (Figures 3C and 3D) and have less hepatic steatosis, as determined by oil red O staining (Figure 3B) and by quantifying total triglycerides (TAGs) (Figure 3E). HFD-fed *Rictor*^{BATKO} mice also have 19% less visceral adipose tissue (VAT) expansion (Figure 3F), 18% less circulating TAGs (Figure S3C), and improved glucose tolerance (Figure S3D). There is an interesting trend of decreased food consumption by *Rictor*^{BATKO} mice, but it is not statistically significant (Figures S3E and S3F). Thus, conditional BAT *Rictor* loss may enhance DIT.

We wondered if inducing *Rictor* deletion in adult mice could achieve the same metabolic benefit. To test this, we generated *Ucp1-creER;Rictor* and *Ucp1-creER* mice and, at 20 weeks of age, briefly administered tamoxifen to generate inducible BAT *Rictor* knockouts and their respective controls (Figure S3G). Mice were then moved to 30°C and kept on SCD, or switched to HFD, for 10 weeks beginning 1 week after acclimatization. Inducible BAT *Rictor*-knockout mice on HFD gain less weight (Figure 3G), maintain histological features of active BAT (Figure 3H), and have less hepatic steatosis (Figure 3H), less VAT expansion (Figure S3H), and less hyperlipidemia (free FAs [FFAs] and TAGs) and hypercholesterolemia (Figure 3I). Their glucose tolerance is also markedly improved (Figure 3J). Thus, inducibly inhibiting BAT mTORC2 also protects against diet-induced obesity.

Inhibiting BAT mTORC2 Stimulates Lipolysis and Lipid Uptake

Next, we examined the molecular signature of thermoneutral housed *Rictor*^{BATKO} on the different diets. HFD attenuates P-AKT1-S473 and P-AKT2-S474 in control BAT, which as expected are impaired in all *Rictor*^{BATKO} mice (Figures 4A and S4A); P-AKT-T308 is difficult to detect under these conditions. Deleting *Rictor* and/or HFD also attenuates SGK1-dependent NDRG1-T346 phosphorylation and NDRG1 total protein (Figures 4A and S4A). Strikingly, the amount of UCP1 mRNA and protein induced by HFD is dramatically amplified in *Rictor*^{BATKO} mice (Figures 4A, 4B, and S4A), indicating that mTORC2 also suppresses UCP1 expression during DIT.

Control and *Rictor*^{BATKO} mice eating SCD express low levels of ACLY, ACC, and FASN (Figures 4A and S4A), consistent with decreased BAT DNL at thermoneutrality (Sanchez-Gurmaches et al., 2018; Trayhurn, 1981). Interestingly, HFD stimulates ACLY, ACC, FASN, and UCP1 expression in control BAT (Figures 4A and S4A) indicating that DIT increases DNL similarly to CIT. Moreover, deleting *Rictor* blocks HFD-induced DNL pathway expression (Figures 4A and S4A), confirming that mTORC2 promotes DNL but also revealing that upregulated DNL is not required for UCP1 upregulation in *Rictor*^{BATKO} mice. This led us to hypothesize that BAT mTORC2 loss may potentiate thermogenesis independently of its role in DNL.

Other thermogenesis and lipid catabolism markers were also examined. *Pgc1a* exhibits the same mRNA signature as *Ucp1* (Figure 4B). In contrast, *Atgl* which encodes the rate-limiting regulator of lipolysis, (Zechner et al., 2012) is elevated in HFD-fed *Rictor*^{BATKO} mice (Figure 4B). The expression of *Irf4* (which encodes a PGC-1α partner) (Kong et al., 2014), *Bnip3* (a mitochondria bioenergetics regulator) (Choi et al., 2016), *Acot4* and *Ehhadh* (FA oxidation regulators) (Schrader et al., 2015), and *Lpl* (a lipase that promotes lipid uptake) (Klingenspor et al., 1996) mirrors *Atgl* expression (Figure 4B). Consistently, ATGL protein level is equivalent between chow-fed control and *Rictor*^{BATKO} mice but significantly higher in HFD *Rictor*^{BATKO} mice compared with HFD-fed controls (Figures 4A and S4A). This suggests that mTORC2 suppresses ATGL-mediated lipolysis in the HFD-fed group, which we confirmed in an *ex vivo* lipolysis assay (Figure 4C). Thus, in addition to its positive role in anabolic DNL, BAT mTORC2 suppresses lipid catabolism, especially during dietary stress.

We also examined lipolytic signaling using the *in vitro Rictor-iKO* brown adipocyte model. In a time course experiment following CL-316,243 treatment, we observe higher basal ATGL levels in unstimulated *Rictor-iKO* cells (i.e., at time 0) compared with isogenic controls (Figure S4B). In contrast, P-HSL and P-Perilipin increase only after 30 min of treatment and to markedly higher levels in the *Rictor-iKO* cells (Figure S4B). HSL and Perilipin hyper-phosphorylation precede UCP1 induction, which occurs around 4–8 h after CL-316,243 treatment (Figure S4B). Cellular cAMP level trend higher in *Rictor-iKO* cells in the basal state but are similar to control upon CL-316,243 stimulation (Figure S4C). The increase in lipolytic signaling functionally corresponds to increased lipolysis (Figure S4D). Thus, inducing brown adipocyte *Rictor* deletion *in vitro* enhances basal ATGL expression, but a stimulus is required to potentiate lipolytic signaling and subsequent UCP1 induction. This may partly explain why

(F) Visceral adipose tissue (VAT) mass of mice in (A) (n = 8–12).
(G) Growth curves of *Rictor*^{BATiKO} (i.e., *Ucp1-CreER;Rictor*) mice and controls living at 30°C and eating either SCD or HFD. *Rictor* deletion was induced at 10 weeks of age with tamoxifen. Mice were then acclimated at 30°C for 1 week before being placed on SCD or HFD; n = 13–18 male mice per group.
(H) Representative H&E (BAT, VAT) and oil red O (liver) staining images from mice in (G). Scale bar, 100 μm.
(I) Blood free fatty acid (FFA), triglyceride (TAG), and cholesterol measurements from mice in (G) (n = 6–8).
(J) Glucose tolerance test (GTT) of mice in (G) after 10 weeks of HFD. SCD, n = 7–9; HFD, n = 7 or 8.
Data are mean ± SEM. Statistical significance was calculated using two-way repeated-measures ANOVA with Tukey's multiple comparisons test (A, G, and J) and two-way ANOVA with Tukey's multiple-comparisons test (C, E, F, I, and J): *$p < 0.05$, **$p < 0.01$, and ***$p < 0.001$ (HFD-control versus HFD-*Rictor*^{BATKO} for A, G, and J; SCD versus HFD, control versus *Rictor*^{BATKO}, or control versus *Rictor*^{BATiKO} for C, E, F, I, and J).

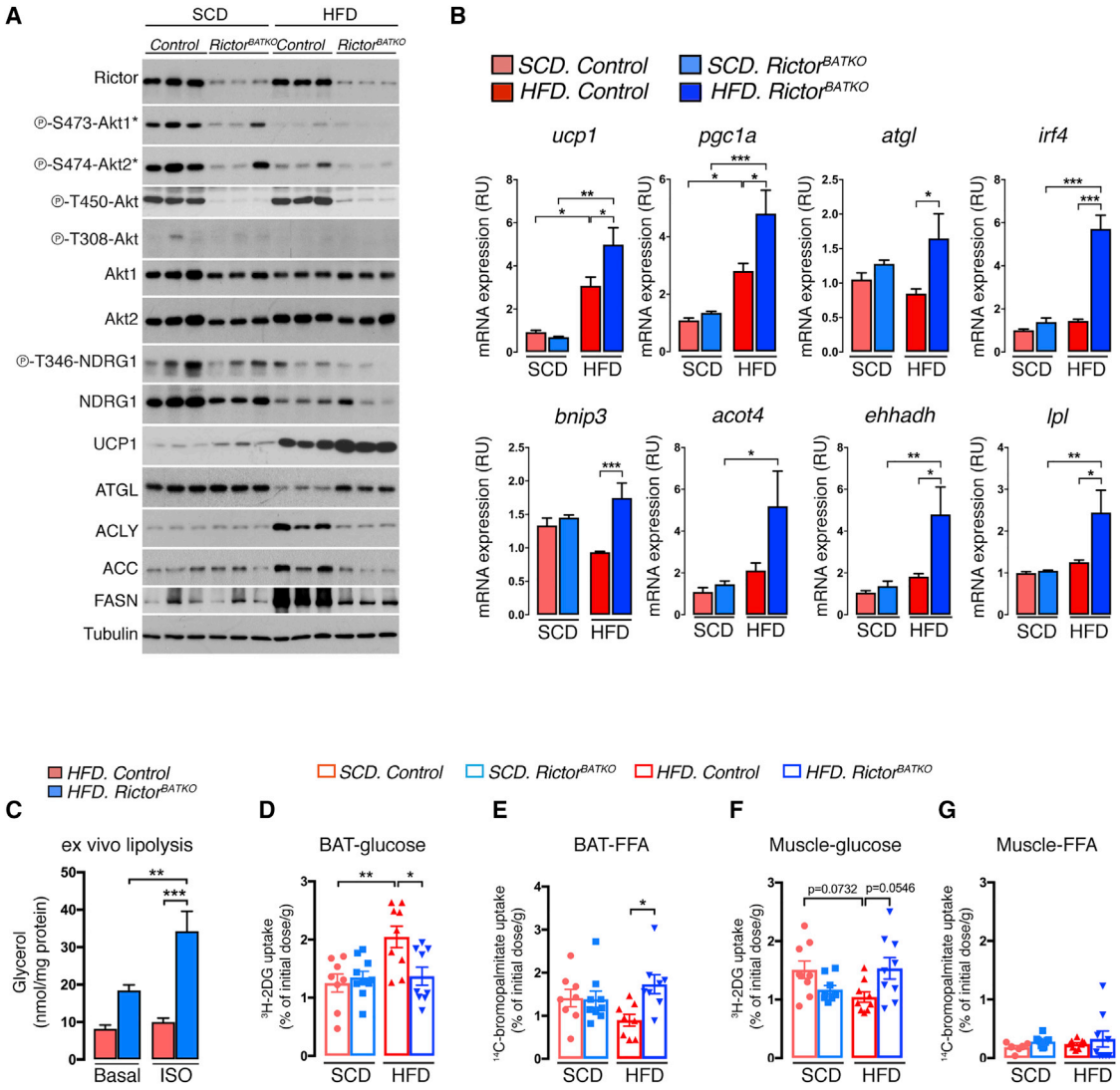

Figure 4. Inhibiting BAT mTORC2 Reprograms Metabolism to Favor Lipid Uptake and Catabolism

(A) Western blot analysis using BAT lysates from mice that were fasted (overnight [O/N]) then refed for 1 h. Mice were living at 30°C and eating SCD or HFD for 8 weeks prior to harvesting the tissue (18-week-old males, n = 3).

(B) qRT-PCR analysis using BAT from mice in (A) (n = 6–8).

(C) *Ex vivo* lipolysis assay, either basal or after isoproterenol (ISO) stimulation, using BAT from *Rictor*^{BATKO} and controls after 8 weeks on HFD at 30°C (n = 8).

(D) *In vivo* ^{3}H-2-deoxy-glucose uptake assay into BAT. Mice were living at 30°C and eating SCD or HFD for 8–16 weeks prior to measuring (n = 8–10).

(E) *In vivo* ^{14}bromo-palmitate uptake assay (n = 8–10).

(F) *In vivo* ^{3}H-2-deoxy-glucose uptake assay into skeletal muscle (quadriceps) (n = 8–10).

(G) *In vivo* ^{14}bromo-palmitate uptake assay into skeletal muscle (quadriceps) (n = 8–10).

Data are mean ± SEM. Statistical significance was calculated using two-way ANOVA with Tukey's multiple-comparisons test (B–G): *p < 0.05, **p < 0.01, and ***p < 0.001 (SCD versus HFD, control versus *Rictor*^{BATKO}, basal versus ISO treated).

Rictor loss has little effect in mice that lack thermal or dietary stress.

Finally, we directly measured nutrient uptake into BAT. In the SCD group, there is no difference between control and *Rictor*^{BATKO} mice in the amount of ^{3}H-2-deoxyglucose or ^{14}C-bromopalmitate taken up by BAT (Figures 4D and 4E). In response to HFD, glucose uptake increases in control BAT by 63% (Figure 4D), while lipid uptake decreases by 37% (Figure 4E), suggesting an increase in *de novo* lipid synthesis upon dietary stress (Figures 4A and S4A). In contrast, HFD has a minimal effect on BAT substrate use in *Rictor*^{BATKO} mice (Figures 4D and 4E), resulting in a nearly 2-fold greater amount of BAT lipid uptake in HFD-fed *Rictor*^{BATKO} mice compared with controls (Figure 4E). The relative increase in lipid uptake is consistent with higher BAT *Lpl* expression in *Rictor*^{BATKO} mice (Figure 4B). Interestingly, the HFD-induced increase in BAT glucose uptake

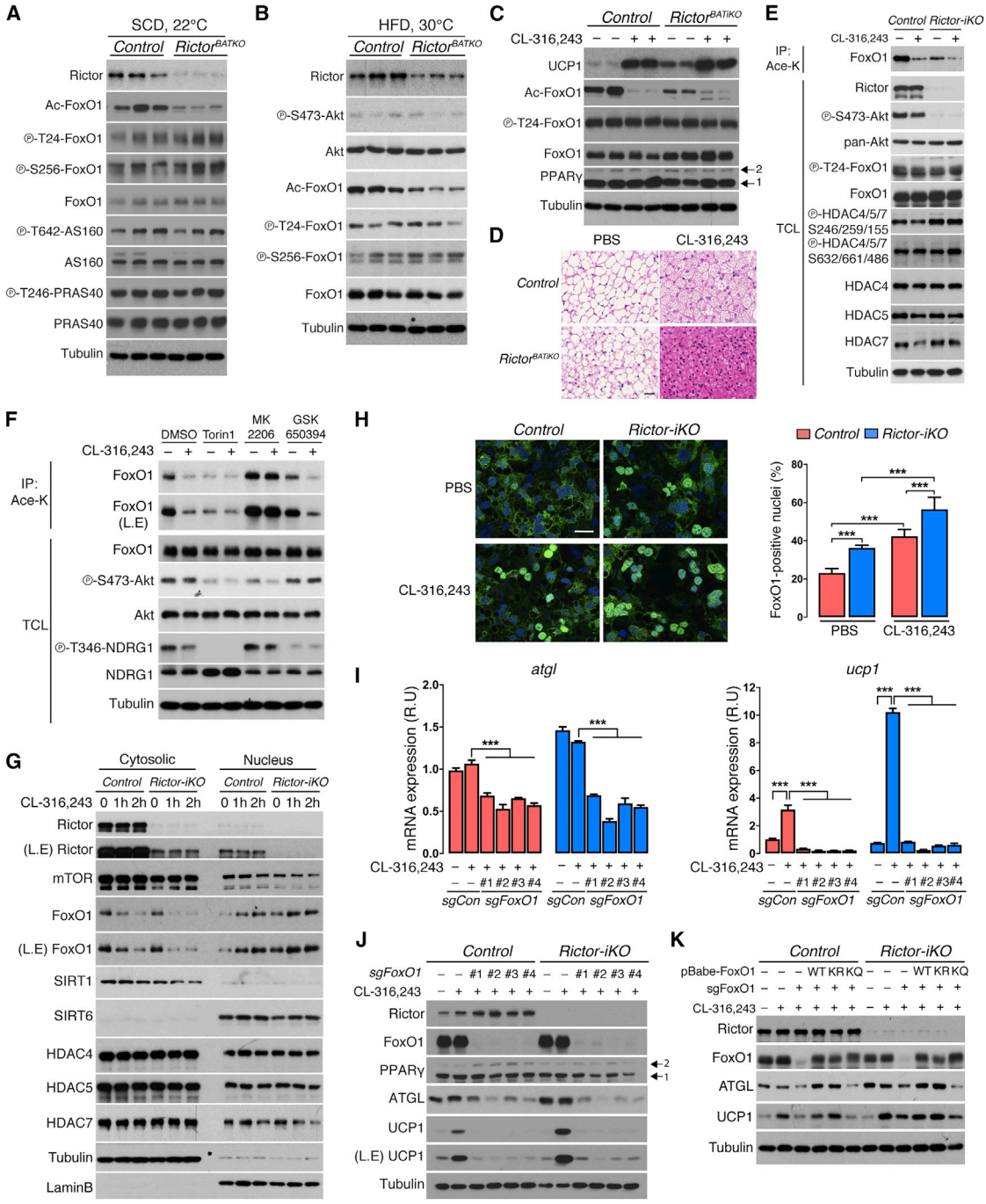

Figure 5. mTORC2 Loss and β-Adrenergic Receptor Signaling Promote FoxO1 Deacetylation and Nuclear Localization

(A) Western blot analysis using BAT lysates from fasted and refed *Rictor*^{BATKO} and control mice living at 22°C and eating SCD (14-week-old males, n = 3).

(B) Western blot analysis using BAT lysates of fasted and refed *Rictor*^{BATKO} and control mice living at 30°C and eating HFD for 8 weeks (18-week-old males, n = 3).

(C) Western blot analysis using BAT from *Rictor*^{BATKO} and control mice living at 30°C treated with PBS or CL-316,243 (0.5 mg/kg, n = 2) for 3 days. Arrows indicate PPARγ isoforms.

(D) Representative H&E staining images from (C). Scale bar, 100 μm.

(E) Immunoprecipitation assay using an anti-acetyl-lysine antibody (Ace-K) and blotting for total FoxO1 from CL-316,243-stimulated (1 μM, 2 h) control and *Rictor-iKO* brown adipocytes. Total cell lysate (TCL) was also probed with the indicated antibodies.

(F) Immunoprecipitation assay as in (E). Cells were pretreated for 1 h with Torin1 (50 nM), MK2206 (0.5 μM), or GSK650394 (1 μM, O/N) followed by CL-316,243 treatment (1 μM, 2 h).

(legend continued on next page)

in control mice is matched by a decrease in glucose uptake by skeletal muscle, and this too is reversed in *Rictor*^{BATKO} mice (Figure 4F). Muscle FFA use is unaffected (Figure 4G). This may contribute to the improved glucose tolerance of these mice (Figure S3D) and confirms that BAT mTORC2 influences system nutrient use. We conclude that mTORC2 balances anabolic and catabolic lipid metabolism to maintain metabolic flexibility and that its absence in BAT removes a brake to lipid catabolism that reprograms systemic nutrient use and potentiates thermogenesis.

Inhibiting mTORC2 Deacetylates and Activates FoxO1 Independently of AKT

Next, we investigated the mechanism by which mTORC2 loss reprograms BAT lipid metabolism. We noted that *Atgl*, *Irf4*, and *Ucp1* expression have been linked to FoxO1, a transcription factor with emerging roles in lipid-related diseases (Chakrabarti and Kandror, 2009; Eguchi et al., 2011; Ortega-Molina et al., 2012; Li et al., 2017). FoxO1 is a classic AKT substrate inhibited by AKT-dependent phosphorylation at T24 and S256 (Manning and Toker, 2017). However, BAT FoxO1 phosphorylation is unaffected in *Rictor*^{BATKO} mice (Figures 5A and 5B). In fact, many AKT target sites, including P-AS160-T642, P-PRAS40-T246, P-GSK3β-S9, and P-TSC2-T1462, are phosphorylated normally when *Rictor* is deleted (Figure 5A) (Hung et al., 2014). Thus, a global AKT signaling defect, and in particular reduced FoxO1 phosphorylation, cannot mechanistically explain the metabolic reprogramming.

A less understood FoxO1 regulatory mechanism is reversible lysine (K) acetylation at six sites (K242, K245, K259, K262, K271, and K291), in which deacetylation is thought to promote nuclear retention and activity (Li et al., 2017). Strikingly, BAT FoxO1 is hypo-acetylated in *Rictor*^{BATKO} mice during both CIT (Figure 5A) and DIT (Figure 5B). FoxO1 deacetylation has not been implicated in thermogenesis; therefore, we administered CL-316,243 to wild-type mice living at thermoneutrality to test whether FoxO1 deacetylation normally occurs upon BAT stimulation. Indeed, FoxO1 is deacetylated following β-adrenergic stimulation (Figures 5C and 5D). Moreover, while deleting *Rictor* deacetylates FoxO1 in the basal unstimulated state (Figure 5C), CL-316,243 synergizes with *Rictor* loss to enhance FoxO1 deacetylation and amplify the β-adrenergic response, indicated by higher UCP1 levels (Figure 5C) and reduced lipid storage (Figure 5D). Thus, FoxO1 is normally deacetylated upon BAT stimulation, and inhibiting mTORC2 appears to establish a pre-thermogenic state by triggering FoxO1 deacetylation in the absence of stimulation.

Mice lacking the major BAT AKT isoform, *Akt2* (i.e., *Akt2*^{BATKO} mice), like *Rictor*^{BATKO} mice, have reduced BAT mass, lipid content, and DNL, while *Akt1*^{BATKO} mice have no obvious phenotype (Sanchez-Gurmaches et al., 2018). However, in contrast to *Rictor*^{BATKO} mice, FoxO1 acetylation is unaffected in *Akt2*^{BATKO} mice (Figure S5A), and neither *Akt2*^{BATKO} nor *Akt1*^{BATKO} mice are resistant to HFD (Figures S5B–S5E), suggesting that mTORC2 loss may promote FoxO1 deacetylation by an AKT-independent mechanism.

mTORC2-dependent FoxO1 regulation by acetylation, independently of AKT, is recapitulated *in vitro*. For example, treating control brown adipocytes with CL-316,243 triggers FoxO1 deacetylation, indicated by less FoxO1 immuno-purification with a pan-Lys-acetylation antibody, without affecting P-AKT-S473 or P-FoxO1-T24 (Figure 5E). Moreover, in *Rictor-iKO* brown adipocytes, FoxO1 is hypo-acetylated without CL-316,243 treatment, and this is further reduced by CL-316,243 without affecting FoxO1 phosphorylation (Figure 5E). We further show that treating brown adipocytes with the mTOR kinase inhibitor Torin1 triggers FoxO1 deacetylation to the same extent as CL-316,243 (Figure 5F), indicating that inhibiting mTOR catalytic activity is sufficient to stimulate FoxO1 deacetylation. Importantly, neither the pan-AKT inhibitor MK-2206 nor the SGK inhibitor GSK-650394 simulates FoxO1 deacetylation (Figure 5F). Interestingly, inhibiting AKT protects against CL-316,243-induced deacetylation, suggesting that there may be complex interplay between FoxO1 phosphorylation and acetylation. Taken together, these data suggest a non-canonical mechanism by which mTORC2 regulates FoxO1 acetylation.

We also examined FoxO1 localization. Control and *Rictor-iKO* cells were treated for 0, 1, and 2 h with CL-316,243, then fractionated into cytosolic and nuclear fractions, where cytoplasmic tubulin and nuclear lamin B were used as markers for purity (Figure 5G). In CL-316,243-treated controls, cytosolic FoxO1 decreases and nuclear FoxO1 accumulates, indicating that β-adrenergic signaling stimulates FoxO1 nuclear localization (Figure 5G). In *Rictor-iKO* cells, nuclear FoxO1 levels are elevated (and cytoplasmic levels depleted) without CL-316,243, and reach higher nuclear levels upon stimulation (Figure 5G), matching the FoxO1 deacetylation profile. We performed immunofluorescence experiments to directly visualize FoxO1 nuclear retention, and consistently, the number of cells with nuclear FoxO1 is similar between CL-316,243-treated control cells and unstimulated *Rictor-iKO* cells (~40%), which is about twice as many compared with the unstimulated controls (Figure 5H). Moreover, combining *Rictor* loss and CL-316,243

(G) Western blot analysis of the cytoplasmic and nuclear fractions of *Rictor-iKO* brown adipocytes and controls treated with CL-316,243 (1 μM) for 1 or 2 h. Tubulin and lamin B are used to control for fraction purity.

(H) Immunofluorescence analysis of control and *Rictor-iKO* brown adipocytes treated with vehicle (PBS) or CL-316,243 (1 μM, 1 h, n = 6). Anti-FoxO1 antibody (green), DAPI (blue), and the corresponding quantification (right panel) is shown. Scale bar, 25 μm.

(I) qRT-PCR analysis from *Rictor-iKO* brown adipocytes and controls, with or without CL-316,243 stimulation and deleted for *FoxO1* by CRISPR/Cas9 using four independent single guide RNAs (sgRNAs) (n = 3).

(J) Corresponding western blot analysis from (I). Arrows indicate the PPARγ isoforms.

(K) Western blot of lysates from control or *Rictor-iKO* brown adipocytes in which endogenous *FoxO1* was deleted *(sgFoxo1)* and cells were reconstituted with FoxO1-WT, FoxO1-6KR, or FoxO1-6KQ mutant constructs.

Data are mean ± SEM. Statistical significance was calculated using two-way ANOVA with Tukey's multiple-comparisons test: *$p < 0.05$, **$p < 0.01$, and ***$p < 0.001$ (PBS versus CL-316,243-treated, control versus *Rictor-iKO*, *sgControl* versus *sgFoxO1*). L.E., long exposure.

increases the number of cells with nuclear FoxO1 to nearly 60% (Figure 5H). Thus, inhibiting mTORC2 promotes FoxO1 nuclear retention.

We also asked whether deleting *Foxo1* by CRISPR/Cas9 (using four independent guides) blocks *Atgl* and *Ucp1* induction upon *Rictor* loss. Indeed, deleting *Foxo1* attenuates *Atgl* and *Ucp1* mRNA (Figure 5I) and protein expression (Figure 5J) in both control and *Rictor-iKO* cells. We performed similar experiments with a FoxO1 inhibitor (FoxOi; AS1842856). At high doses (2.5–10 μM), FoxO1i blocks *Ucp1* induction in both control and *Rictor-iKO* cells, while at a lower dose (1 μM), inhibition is more specific to *Rictor-iKO* cells (Figure S5F). We also generated primary *adiponectin-Cre;FoxO1* brown adipocytes and confirm in an independent system that ATGL and UCP1 expression, but not PPARγ or ACLY, require FoxO1 (Figure S5G). Finally, we reconstituted *FoxO1*-deleted brown adipocytes with recombinant wild-type FoxO1, acetylation deficient FoxO1 (6KR), or an acetylation mimetic FoxO1 (6KQ) (Figure 5K). Wild-type FoxO1 and FoxO1-6KR both rescue ATGL and UCP1 expression in the *FoxO1*-deleted cells, whereas FoxO1-6KQ cannot, consistent with acetylation inhibiting *Atgl* and *Ucp1* expression. Moreover, only the wild-type and FoxO1-6KR constructs, and not the FoxO1-6KQ construct, up-regulate ATGL and UCP1 in *Rictor-iKO* cells in which endogenous *Foxo1* is deleted (Figure 5K). We conclude that FoxO1 deacetylation promotes *Atgl* and *Ucp1* upregulation upon mTORC2 loss.

SIRT6 Interacts with mTORC2 and Promotes FoxO1 Deacetylation

To identify the FoxO1 deacetylase in mTORC2-deficient brown adipocytes, we first considered class IIa HDACs because two previous studies linked them to FoxO1 (Mihaylova et al., 2011; Masui et al., 2013). The more recent study proposed that mTORC2 controls metabolism through HDAC4/5/7 phosphorylation in glioblastoma cells. Using the same phospho-specific antibodies, and also blotting for total HDAC4/5/7 protein, we do not detect any changes in P-HDAC4/5/7-S246/259/155 or P-HDAC4/5/7-S632/661/486 in control or *Rictor*-deficient BAT or in *Rictor-iKO* brown adipocytes and their isogenic control under the same conditions in which FoxO1 is deacetylated and UCP1 expression is potentiated (Figures 5E and S6A–S6C). Although most HDAC4/5/7 is cytoplasmic in brown adipocytes, a sub-fraction is nuclear; however, we see no HDAC redistribution in response to CL-316,243 and/or *Rictor* loss (Figure 5G). The class II HDAC inhibitor LMK-235 also fails to prevent FoxO1 deacetylation induced by CL-316,243 and/or *Rictor* deletion (Figure S6D). Finally, CRISPR-mediated double or triple knockout of class II HDACs (HDAC4/7, HDAC4/5, HDAC4/5/7) does not prevent FoxO1 deacetylation in response to CL-316,243 stimulation and/or *Rictor* loss (Figure S6E). These data are inconsistent with class IIa HDACs being the FoxO1 deacetylase.

We also considered sirtuins. SIRT1 and SIRT6 are predicted to be nuclear (Houtkooper et al., 2012); however, in brown adipocytes, SIRT1 is predominantly cytoplasmic, while SIRT6 is mainly nuclear (Figure 5G). Using CRISPR/Cas9, we deleted *Sirt6*, *Sirt1*, and the mitochondrial sirtuin *Sirt3* with three independent guides in CL-316,243-stimulated *Rictor-iKO* brown adipocytes. Although the combination of *Rictor* loss and CL-316,243 results in near complete FoxO1 deacetylation (Figure 6A, lane 3), this is completely prevented by deleting *Sirt6* (Figure 6A, lanes 4–6), and deleting *Sirt1* or *Sirt3* has no effect (Figure 6A, lanes 7–12). Consistently, deleting *Sirt6* attenuates ATGL and UCP1 upregulation in *Rictor-iKO* cells (Figure 6B). Furthermore, deleting SIRT6, but not SIRT1, also prevents CL-316,243-stimulated FoxO1 deacetylation in control cells (Figure S6F). These data implicate SIRT6 as the FoxO1 deacetylase whose activity is enhanced by mTORC2 loss.

Consistent with SIRT6 being the FoxO1 deacetylase, we detect endogenous SIRT6 in immuno-precipitates (IPs) with endogenous FoxO1 (Figure 6C). Moreover, the amount of FoxO1 in SIRT6 IPs increases with CL-316,243 treatment, or *Rictor* deletion, and to a greater extent when CL-316,243 and *Rictor* deletion are combined (Figure 6C). The dynamics of the endogenous SIRT6-FoxO1 interaction precisely mirrors the FoxO1 deacetylation and nuclear retention profiles (Figures 5E, 5G, and 5H) supporting SIRT6 as the FoxO1 deacetylase. SIRT6 is also a histone deacetylase, and consistent with mTORC2 suppressing SIRT6 activity, its reported histone targets (H3K9 and H3K56) are also hypo-acetylated in *Rictor-iKO* cells (Figure S6G) (Michishita et al., 2009; Yang et al., 2009; Zhong et al., 2010). This suggests that mTORC2 might also have epigenetic functions.

We noticed in cell fractionation experiments that some Rictor and mTOR protein co-localize in the nucleus with SIRT6 and FoxO1 (Figure 5G). This led us to wonder if mTORC2 and SIRT6 physically interact. Indeed, a fraction of endogenous Rictor and mTOR, but not Raptor, coIPs with endogenous SIRT6 (Figure 6D). Notably, deleting *Rictor* reduces the amount of mTOR detected in SIRT6 IP; however, some mTOR remains in the SIRT6 immune complexes (Figure 6D). Reciprocally, endogenous mTOR IPs recover endogenous SIRT6 and Rictor, but not SIRT1. Interestingly, the amount of SIRT6 recovered in mTOR IPs is unaffected by deleting *Rictor* and destabilized by CL-316,243 (Figure 6E). Thus, SIRT6 may associate with mTOR independently of Rictor. Finally, using the HaloTag affinity purification system followed by mass spectrometry (MS) analysis, mTOR, RICTOR, SIN1 (another mTORC2 subunit), and TTI1 and TEL2 (mTORC2 assembly factors; Kaizuka et al., 2010) were identified as SIRT6 interactors in HEK293 and HeLa cells (Figures 6F and S6H; Table S1). We confirmed the endogenous interaction between human SIRT6 and mTORC2 by co-immunoprecipitation in both cell lines (Figures 6G and S6I). Thus, mTORC2 appears to interact with SIRT6 in diverse mouse and human cells.

mTORC2 Regulates Lipid Anabolism and Catabolism through Different Pathways

To test the *in vivo* relevance of FoxO1 downstream of *Rictor* loss, we generated *Ucp1-Cre;FoxO1* (*FoxO1*^{BATKO}) single-knockout and *Ucp1-Cre;Rictor;FoxO1* (*FoxO1;Rictor*^{BATDKO}) double-knockout mice. Overall, *FoxO1*^{BATKO} mice living at 22°C are similar in weight to controls, although BAT and WAT mass trend slightly larger (Figure S7A); this correlates with increased BAT lipid droplet size (Figure 7A). No differences are observed in other tissues (Figure S7A). BAT *Atgl* and *Irf4* mRNA (Figure 7B) and ATGL protein levels (Figures 7C and S7C) are reduced in

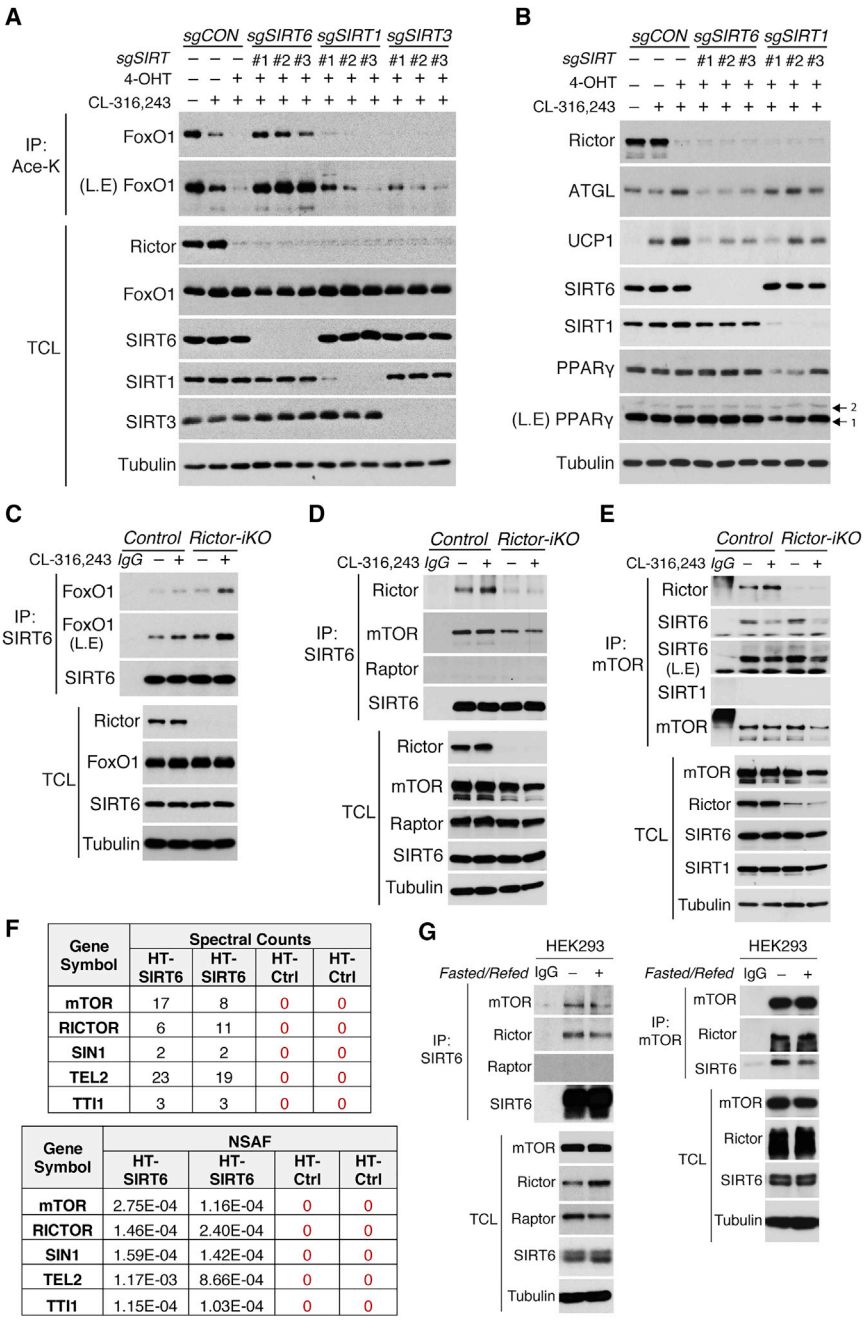

F

Gene Symbol	Spectral Counts			
	HT-SIRT6	HT-SIRT6	HT-Ctrl	HT-Ctrl
mTOR	17	8	0	0
RICTOR	6	11	0	0
SIN1	2	2	0	0
TEL2	23	19	0	0
TTI1	3	3	0	0

Gene Symbol	NSAF			
	HT-SIRT6	HT-SIRT6	HT-Ctrl	HT-Ctrl
mTOR	2.75E-04	1.16E-04	0	0
RICTOR	1.46E-04	2.40E-04	0	0
SIN1	1.59E-04	1.42E-04	0	0
TEL2	1.17E-03	8.66E-04	0	0
TTI1	1.15E-04	1.03E-04	0	0

Figure 6. SIRT6 Interacts with mTORC2 and FoxO1 and Is Necessary for FoxO1 Deacetylation upon β-Adrenergic Stimulation or *Rictor* Loss

(A) Immunoprecipitation assay using an anti-acetyl-lysine antibody (Ace-K) and blotting for total FoxO1 from CL-316,243-stimulated (1 μM, 2 h) *Rictor-iKO* brown adipocytes in which SIRT6, SIRT1, and SIRT3 were also ablated by CRISPR/Cas9 using three independent sgRNAs each.

(B) Western blot analysis of CL-316,243-stimulated (1 μM, 8 h) *Rictor-iKO* brown adipocytes expressing three independent sgRNAs each targeting SIRT6 or SIRT1.

(C) Endogenous SIRT6 immunoprecipitation (IP) from control and *Rictor-iKO* brown adipocytes under basal, CL-316,243-stimulated (1 μM, 2 h), *Rictor*-deleted, or combined CL-316,243 and *Rictor*-deleted conditions. Endogenous FoxO1 is also probed in the SIRT6 IP.

(D) Endogenous SIRT6 immunoprecipitation (IP) from control and *Rictor-iKO* brown adipocytes. Cells were stimulated with CL-316,243 (1 μM, 2 h). Endogenous Rictor and mTOR are also probed in the SIRT6 IP.

(E) Endogenous mTOR immunoprecipitation (IP) from control and *Rictor-iKO* brown adipocytes as in (D). Endogenous Rictor and SIRT6 are also probed in the mTOR IP.

(F) Affinity pull-down-MS data from HaloTag SIRT6-expressing HEK293 cells identifying mTORC2 subunits (mTOR, Rictor, Sin1) and assembly factors (Tel2, TTI1) as SIRT6 interactors (see also STAR Methods). Spectral counts (SpC) and normalized spectral abundance factors (NSAFs) from two biological replicates are shown for HaloTag SIRT6 and HaloTag-alone control.

(G) Endogenous SIRT6 IP (left) and mTOR IP (right) using HEK293 lysates. IgG is the negative control. Cells were treated with no medium change (Fasted/Refed-) or starved with 0.5% FBS for 6h followed by refeeding with 10% FBS for 0.5h (Fasted/Refed+). L.E., long exposure; TCL, total cell lysate.

FoxO1^{BATKO} mice, consistent with their predicted roles as FoxO1 targets. Expression of *Pgc1a* trends lower (Figure 7B), while *Ucp1* mRNA is unchanged (Figure 7B), and UCP1 protein barely decreases (Figures 7C and S7C). A broader analysis of predicted FoxO1 target genes only further identifies *Lpl* and *Bnip3* as being significantly reduced under these conditions (Figure S7B). The DNL pathway (i.e., ACLY, ACC, and FASN expression) is unaffected by *FoxO1* loss (Figures 7C and S7C). Thus, in mild cold-adapted mice, deleting BAT *FoxO1* affects mainly lipid uptake and lipolysis regulators but not the DNL pathway or UCP1.

Next, we removed thermal stress by acclimating *Ucp1-Cre;FoxO1* and control mice to 30°C, then stimulated them with CL-316,243 to induce thermogenesis. Without thermal stress, both the control and *Ucp1-Cre;FoxO1* brown adipocytes are morphologically similar (Figure 7D). As expected, CL-316,243 potently stimulates BAT activity in controls, indicated by dramatic lipid depletion (Figure 7D), increased UCP1 levels (Figure 7E), and increased ACLY and ACC expression (Figure 7E). Deleting *FoxO1* partially attenuates CL-316,243-induced lipid depletion (Figure 7D), further depletes ATGL levels (Figure 7E), and partially blocks UCP1 induction (Figure 7E) but has no effect on ACLY or ACC induction (Figure 7E). Thus, BAT FoxO1 is normally required downstream of β-adrenergic signaling to maximally stimulate UCP1 expression, but not to induce DNL.

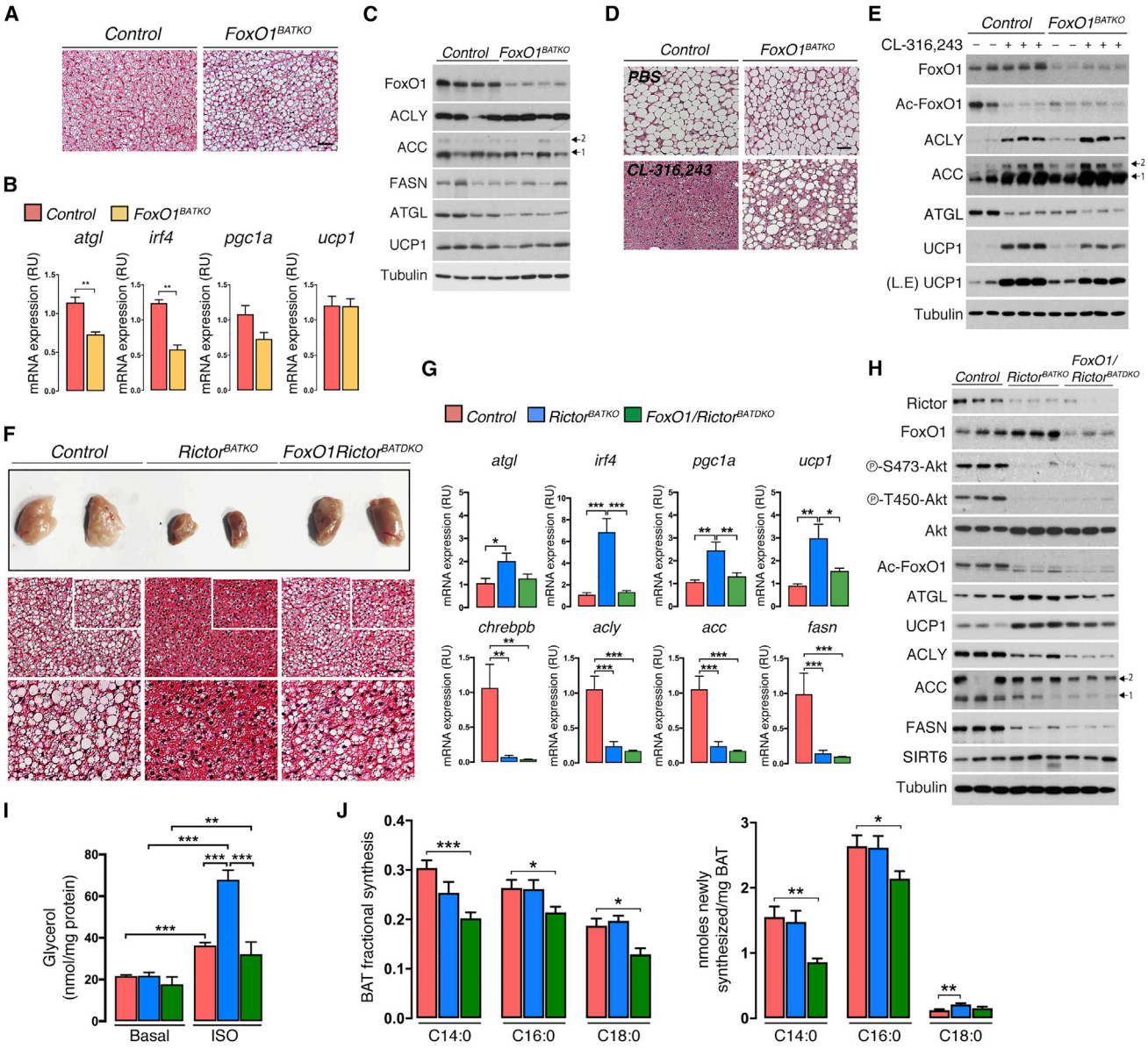

Figure 7. FoxO1 Reprograms Catabolic, but Not Anabolic, Lipid Metabolism upon mTORC2 Loss *In Vivo*

(A) Representative H&E staining images of BAT from *FoxO1*^{BATKO} and controls under standard condition (22°C, SCD, 8-week-old males). Scale bar, 100 μm.

(B) qRT-PCR analysis using BAT from fasted and refed *FoxO1*^{BATKO} and control mice at (22°C, SCD, 8-week-old males, n = 5 or 6).

(C) Western blot analysis corresponding to (B) (8-week-old males, n = 4).

(D) Representative H&E staining images of BAT from *FoxO1*^{BATKO} and control mice living at 30°C and treated with PBS or CL-316,243 (0.5 mg/kg) for 3 days.

(E) Corresponding western blot analysis for (D); n = 2 or 3.

(F) Representative photograph and H&E staining images of BAT from control, *Rictor* ^{BATKO}, and *FoxO1;Rictor*^{BATDKO} mice under standard conditions (8-week-old males, n = 5 or 6). White box inset corresponds to the enlarged H&E images below. Scale bar, 100 μm.

(G) qRT-PCR analysis of BAT from (F) (8-week-old males, n = 6–8).

(H) Western blot analysis for (G), (8-week-old males, n = 3).

(I) *Ex vivo* lipolysis assay of BAT under basal or isoproterenol (ISO)-stimulated conditions (22°C, SCD, 8-week-old males, n = 8).

(J) Heavy water (D_2O) labeling showing the fraction (left) and quantification (right) of *de novo* synthesized fatty acid species (C14:0, C16:0, C18:0) in BAT (22°C, SCD, 8-week-old males, n = 6–9).

Data are mean ± SEM. Statistical significance was calculated using the Mann-Whitney test (B), one-way ANOVA with Tukey's multiple-comparisons test (G), two-way ANOVA with Tukey's multiple-comparisons test (I), and multiple t test (J): *p < 0.05, **p < 0.01, and ***p < 0.001 (control versus *FoxO1*^{BATKO}, control versus *Rictor*^{BATKO} versus *FoxO1/Rictor*^{BATDKO}, basal versus ISO treated).

Finally, we used *FoxO1;Rictor*^{BATDKO} mice to ask if FoxO1 is required for BAT metabolic reprogramming when mTORC2 is inhibited. Remarkably, BAT mass and lipid droplet size are mostly restored in *FoxO1;Rictor*^{BATDKO} mice (Figures 7F and S7D), and *Atgl*, *Irf4*, *Pgc1α*, *Ucp1*, and *Lpl* mRNA expression are normalized to near control levels (Figures 7G and S7E). Deleting *Rictor* also induces FoxO1-dependent *p21* expression, which was unaffected in *FoxO1* single-knockout mice (Figure S7E). Western blots confirm *Rictor* and *FoxO1* deletion and that deleting *FoxO1* fully reverts ATGL and partially reverts UCP1 to control levels in *Rictor*-deficient BAT (Figures 7H, S7F, and S7G). *Ex vivo* lipolysis measurements functionally confirm restoration of lipolytic control in the double knockout (Figure 7I), indicating that FoxO1 unilaterally drives ATGL expression and that additional factors likely cooperate with FoxO1 to induce UCP1.

In contrast, *Chrebpβ*, *Acly*, *Acc*, and *Fasn* levels remain strongly attenuated in both the *Rictor*^{BATKO} and *FoxO1;Rictor*^{BATDKO} mice (Figure 7G) indicating that *FoxO1* loss does not rescue the DNL pathway in *Rictor*-deficient BAT. We confirmed this by western blotting for ACLY, ACC, and FASN (Figures 7H, S7F, and S7G). To functionally confirm this, we performed *in vivo* D_2O labeling to quantify *de novo* synthesized lipids in BAT. No significant difference in D_2O labeling is observed between control and *Rictor*^{BATDKO} mice (Figure 7J), which was not unexpected because *Rictor*-deficient BAT has higher lipid uptake (Figures 4E and S7H), and this technique does not distinguish locally synthesized lipids from those synthesized in other tissues and absorbed from circulation. *In vitro*, however, acute *Rictor* loss decreases DNL by 45% (Figure S7I). If the hypothesis is correct, then deleting *FoxO1* in addition to *Rictor* should reverse lipid uptake and catabolism, thereby revealing the endogenous DNL defect. This is indeed the case; the amount of D_2O labeled myristic acid (C14:0), palmitic acid (C16:0), and stearic acid (C18:0) significantly decreases in the *FoxO1;Rictor*^{BATDKO} mice (Figure 7J), consistent with *Lpl* levels returning to normal (Figure S7E), and the DNL pathway remaining downregulated (Figures 7G, 7H, S7F, and S7G). Thus, we propose a model in which BAT mTORC2 balances anabolic and catabolic lipid metabolism through distinct pathways, and that SIRT6 drives FoxO1 deacetylation and lipid catabolism downstream of mTORC2 loss.

DISCUSSION

BAT is an attractive therapeutic target against obesity and its comorbidities because of its ability to expend energy by NST (Harms and Seale, 2013). Here, we describe a novel mouse model with enhanced BAT activity that protects against overnutrition and cold temperature and is driven solely by inhibiting mTORC2 in mature brown adipocytes. We provide evidence of a mechanism in which mTORC2 loss triggers the deacetylation and activation of FoxO1 through SIRT6 in a non-canonical mTORC2 pathway. This appears to lower a transcriptional barrier to adaptive thermogenesis thereby potentiating β-adrenergic stimulation in response to thermal or dietary stress.

An interesting finding from studying brown and white adipocyte mTORC2 (Hung et al., 2014; Tang et al., 2016) is that although conditionally deleting *Rictor* profoundly alters metabolism, it appears to do so independently of a major global AKT signaling defect. At least three models that are not necessarily mutually exclusive could explain this: (1) following prolonged mTORC2 loss, AKT signaling reprograms to become mTORC2 independent, (2) mTORC2 is more essential for an unidentified subset of AKT functions, or (3) mTORC2 has AKT-independent roles in metabolism. Losing *Rictor* in adipocytes does not affect mTORC1 activity, nor the ability to stimulate AKT signaling with physiological levels of insulin (Hung et al., 2014; Tang et al., 2016) arguing against compensation by negative feedback or hyperinsulinemia. Lack of an acute and selective mTORC2 inhibitor currently precludes our ability to further test the first model, and although our findings do not rule out the possibility that mTORC2 regulates specific AKT substrates, the data in this study support the latter hypothesis that mTORC2 can regulate lipid catabolism by AKT (and SGK)-independent pathways. The fact that double deletion of *FoxO1* and *Rictor* normalizes ATGL and partially rescues UCP1 expression, but not DNL, also supports the notion that mTORC2 controls lipid anabolism and catabolism by different mechanisms. The former may be AKT dependent given that *Akt2*^{BATKO} mice have a DNL defect (Sanchez-Gurmaches et al., 2018). Defining the acute, essential, and specific roles of mTORC2 in AKT signaling and metabolism remain important goals.

Another future goal is to understand how mTORC2 regulates SIRT6. The low K_m of SIRT6 for NAD^+ (26 μM) makes it unlikely that NAD^+ availability regulates SIRT6 (Cantó et al., 2015; Pan et al., 2011). SIRT6 activity is stimulated by specific lipids (Feldman et al., 2013), whose availability could be regulated by mTORC2. The finding that sub-stoichiometric amounts of SIRT6 co-immunoprecipitate with mTORC2 suggests regulation could be direct, for example, by sequestering or phosphorylating SIRT6, although the interaction could also exist through a higher order complex that survives immuno-purification. An interesting speculation is that the interaction between mTORC2 and SIRT6 is mediated by a nuclear mTORC2, which has been predicted (Rosner and Hengstschläger, 2008), but for which no function is assigned. Alternatively, mTORC2 could promote lysine acetyl transferase (KAT) activity toward FoxO1 that counters SIRT6's deacetylase activity (Pietrocola et al., 2015). Whether SIRT6 histone deacetylase activity (Zhong et al., 2010; Kim et al., 2010) or other unidentified SIRT6 substrates also contribute to metabolic reprogramming upon mTORC2 loss is another key question.

In sum, our data suggest a novel mechanism by which brown fat mTORC2 controls catabolic lipid metabolism independently of the canonical mTORC2-AKT paradigm to regulate thermogenesis and whole-body lipid storage. This mechanism is likely conserved in other tissues and should be explored for its clinical relevance in metabolic diseases and cancer.

STAR★METHODS

Detailed methods are provided in the online version of this paper and include the following:

- KEY RESOURCES TABLE
- LEAD CONTACT AND MATERIALS AVAILABILITY
- EXPERIMENTAL MODEL AND SUBJECT DETAILS
  - Mice
  - Cell culture

SUPPLEMENTAL INFORMATION

Supplemental Information can be found online at https://doi.org/10.1016/j.molcel.2019.07.023.

ACKNOWLEDGMENTS

We thank Mathieu Laplante for advice with nutrient uptake experiments, Christian Wolfrum for Ucp1-CreER mice, Evan Rosen for Adiponectin-Cre and Ucp1-Cre mice, Morrie Birnbaum for AKT floxed mice, and Jessica Feldman for technical advice. This work was supported by grants from the NIH (R01DK094004 and R01CA196986) and a Leukemia and Lymphoma Society Career Development Award to D.A.G. S.M.J. is supported by a postdoctoral fellowship from the American Diabetes Association (1-18-PDF-128). J.S.-G. was supported by a postdoctoral fellowship from the American Heart Association (15POST25550079). C.M.C. was supported by a postdoctoral fellowship from the American Diabetes Association (1-16-PMF-008). C.M.M. is supported by a grant from the NIH (R01CA188652). A.K.L. is supported by a post-doctoral fellowship from the American Cancer Society (PF-19-103-01-TBE).

AUTHOR CONTRIBUTIONS

C.-M.H., S.M.J., and D.A.G. conceptualized the study, designed the experiments, and interpreted the data. S.M.J. performed most of the experiments with assistance from C.-M.H., S.R.H., and D.M. J.S.-G. performed the experiments with *AKT*^{floxed} mice. J.M.G., M.W., and C.M.M. performed and analyzed D_2O incorporation experiments. C.M.C. and A.K.L. assisted with biochemical analyses. Y.T. and W.-Y.H. assisted with mouse metabolic phenotyping. B.M.-P., D.L.D., and R.M. performed and analyzed the HaloTag affinity purification and MS experiments. H.L. assisted with animal husbandry and genotyping. S.M.J. and D.A.G. wrote the manuscript.

DECLARATION OF INTERESTS

The authors declare no conflicts of interest.

Received: April 15, 2019
Revised: May 30, 2019
Accepted: July 15, 2019
Published: August 22, 2019

REFERENCES

Barquissau, V., Beuzelin, D., Pisani, D.F., Beranger, G.E., Mairal, A., Montagner, A., Roussel, B., Tavernier, G., Marques, M.A., Moro, C., et al. (2016). White-to-brite conversion in human adipocytes promotes metabolic reprogramming towards fatty acid anabolic and catabolic pathways. Mol. Metab. *5*, 352–365.

Cannon, B., and Nedergaard, J. (2004). Brown adipose tissue: function and physiological significance. Physiol. Rev. *84*, 277–359.

Cannon, B., and Nedergaard, J. (2011). Nonshivering thermogenesis and its adequate measurement in metabolic studies. J. Exp. Biol. *214*, 242–253.

Cantó, C., Menzies, K.J., and Auwerx, J. (2015). NAD(+) metabolism and the control of energy homeostasis: a balancing act between mitochondria and the nucleus. Cell Metab. *22*, 31–53.

Chakrabarti, P., and Kandror, K.V. (2009). FoxO1 controls insulin-dependent adipose triglyceride lipase (ATGL) expression and lipolysis in adipocytes. J. Biol. Chem. *284*, 13296–13300.

Choi, J.W., Jo, A., Kim, M., Park, H.S., Chung, S.S., Kang, S., and Park, K.S. (2016). BNIP3 is essential for mitochondrial bioenergetics during adipocyte remodelling in mice. Diabetologia *59*, 571–581.

Deberardinis, R.J., Lum, J.J., and Thompson, C.B. (2006). Phosphatidylinositol 3-kinase-dependent modulation of carnitine palmitoyltransferase 1A expression regulates lipid metabolism during hematopoietic cell growth. J. Biol. Chem. *281*, 37372–37380.

Eguchi, J., Wang, X., Yu, S., Kershaw, E.E., Chiu, P.C., Dushay, J., Estall, J.L., Klein, U., Maratos-Flier, E., and Rosen, E.D. (2011). Transcriptional control of adipose lipid handling by IRF4. Cell Metab. *13*, 249–259.

Eissing, L., Scherer, T., Tödter, K., Knippschild, U., Greve, J.W., Buurman, W.A., Pinnschmidt, H.O., Rensen, S.S., Wolf, A.M., Bartelt, A., et al. (2013). De novo lipogenesis in human fat and liver is linked to ChREBP-β and metabolic health. Nat. Commun. *4*, 1528.

Facchinetti, V., Ouyang, W., Wei, H., Soto, N., Lazorchak, A., Gould, C., Lowry, C., Newton, A.C., Mao, Y., Miao, R.Q., et al. (2008). The mammalian target of rapamycin complex 2 controls folding and stability of Akt and protein kinase C. EMBO J. *27*, 1932–1943.

Fasshauer, M., Klein, J., Kriauciunas, K.M., Ueki, K., Benito, M., and Kahn, C.R. (2001). Essential role of insulin receptor substrate 1 in differentiation of brown adipocytes. Mol. Cell. Biol. *21*, 319–329.

Feldman, M.E., Apsel, B., Uotila, A., Loewith, R., Knight, Z.A., Ruggero, D., and Shokat, K.M. (2009). Active-site inhibitors of mTOR target rapamycin-resistant outputs of mTORC1 and mTORC2. PLoS Biol. *7*, e38.

Feldman, J.L., Baeza, J., and Denu, J.M. (2013). Activation of the protein deacetylase SIRT6 by long-chain fatty acids and widespread deacylation by mammalian sirtuins. J. Biol. Chem. *288*, 31350–31356.

Feldmann, H.M., Golozoubova, V., Cannon, B., and Nedergaard, J. (2009). UCP1 ablation induces obesity and abolishes diet-induced thermogenesis in mice exempt from thermal stress by living at thermoneutrality. Cell Metab. *9*, 203–209.

Fernandez, C.A., Des Rosiers, C., Previs, S.F., David, F., and Brunengraber, H. (1996). Correction of 13C mass isotopomer distributions for natural stable isotope abundance. J. Mass Spectrom. *31*, 255–262.

Fischer, A.W., Schlein, C., Cannon, B., Heeren, J., and Nedergaard, J. (2019). Intact innervation is essential for diet-induced recruitment of brown adipose tissue. Am. J. Physiol. Endocrinol. Metab. *316*, E487–E503.

Fisher, F.M., Kleiner, S., Douris, N., Fox, E.C., Mepani, R.J., Verdeguer, F., Wu, J., Kharitonenkov, A., Flier, J.S., Maratos-Flier, E., and Spiegelman, B.M. (2012). FGF21 regulates PGC-1α and browning of white adipose tissues in adaptive thermogenesis. Genes Dev. *26*, 271–281.

Gaubitz, C., Prouteau, M., Kusmider, B., and Loewith, R. (2016). TORC2 structure and function. Trends Biochem. Sci. *41*, 532–545.

Gordon, C.J., Aydin, C., Repasky, E.A., Kokolus, K.M., Dheyongera, G., and Johnstone, A.F. (2014). Behaviorally mediated, warm adaptation: a physiological strategy when mice behaviorally thermoregulate. J. Therm. Biol. *44*, 41–46.

Guertin, D.A., Stevens, D.M., Thoreen, C.C., Burds, A.A., Kalaany, N.Y., Moffat, J., Brown, M., Fitzgerald, K.J., and Sabatini, D.M. (2006). Ablation in mice of the mTORC components raptor, rictor, or mLST8 reveals that mTORC2 is required for signaling to Akt-FOXO and PKCalpha, but not S6K1. Dev. Cell *11*, 859–871.

Harms, M., and Seale, P. (2013). Brown and beige fat: development, function and therapeutic potential. Nat. Med. *19*, 1252–1263.

Herman, M.A., Peroni, O.D., Villoria, J., Schön, M.R., Abumrad, N.A., Blüher, M., Klein, S., and Kahn, B.B. (2012). A novel ChREBP isoform in adipose tissue regulates systemic glucose metabolism. Nature *484*, 333–338.

Houtkooper, R.H., Pirinen, E., and Auwerx, J. (2012). Sirtuins as regulators of metabolism and healthspan. Nat. Rev. Mol. Cell Biol. *13*, 225–238.

Hung, C.M., Calejman, C.M., Sanchez-Gurmaches, J., Li, H., Clish, C.B., Hettmer, S., Wagers, A.J., and Guertin, D.A. (2014). Rictor/mTORC2 loss in the Myf5 lineage reprograms brown fat metabolism and protects mice against obesity and metabolic disease. Cell Rep. *8*, 256–271.

Hylander, B.L., and Repasky, E.A. (2016). Thermoneutrality, mice, and cancer: a heated opinion. Trends Cancer *2*, 166–175.

Jacinto, E., Facchinetti, V., Liu, D., Soto, N., Wei, S., Jung, S.Y., Huang, Q., Qin, J., and Su, B. (2006). SIN1/MIP1 maintains rictor-mTOR complex integrity and regulates Akt phosphorylation and substrate specificity. Cell *127*, 125–137.

Kaizuka, T., Hara, T., Oshiro, N., Kikkawa, U., Yonezawa, K., Takehana, K., Iemura, S., Natsume, T., and Mizushima, N. (2010). Tti1 and Tel2 are critical factors in mammalian target of rapamycin complex assembly. J. Biol. Chem. *285*, 20109–20116.

Kim, H.S., Xiao, C., Wang, R.H., Lahusen, T., Xu, X., Vassilopoulos, A., Vazquez-Ortiz, G., Jeong, W.I., Park, O., Ki, S.H., et al. (2010). Hepatic-specific disruption of SIRT6 in mice results in fatty liver formation due to enhanced glycolysis and triglyceride synthesis. Cell Metab. *12*, 224–236.

Klingenspor, M., Ebbinghaus, C., Hülshorst, G., Stöhr, S., Spiegelhalter, F., Haas, K., and Heldmaier, G. (1996). Multiple regulatory steps are involved in the control of lipoprotein lipase activity in brown adipose tissue. J. Lipid Res. *37*, 1685–1695.

Kong, X., Banks, A., Liu, T., Kazak, L., Rao, R.R., Cohen, P., Wang, X., Yu, S., Lo, J.C., Tseng, Y.H., et al. (2014). IRF4 is a key thermogenic transcriptional partner of PGC-1α. Cell *158*, 69–83.

Kontani, Y., Wang, Y., Kimura, K., Inokuma, K.I., Saito, M., Suzuki-Miura, T., Wang, Z., Sato, Y., Mori, N., and Yamashita, H. (2005). UCP1 deficiency increases susceptibility to diet-induced obesity with age. Aging Cell *4*, 147–155.

Labbé, S.M., Mouchiroud, M., Caron, A., Secco, B., Freinkman, E., Lamoureux, G., Gélinas, Y., Lecomte, R., Bossé, Y., Chimin, P., et al. (2016). mTORC1 is required for brown adipose tissue recruitment and metabolic adaptation to cold. Sci. Rep. *6*, 37223.

Leavens, K.F., Easton, R.M., Shulman, G.I., Previs, S.F., and Birnbaum, M.J. (2009). Akt2 is required for hepatic lipid accumulation in models of insulin resistance. Cell Metab. *10*, 405–418.

Lee, W.N., Bassilian, S., Ajie, H.O., Schoeller, D.A., Edmond, J., Bergner, E.A., and Byerley, L.O. (1994). In vivo measurement of fatty acids and cholesterol synthesis using D2O and mass isotopomer analysis. Am. J. Physiol. *266*, E699–E708.

Lee, W.N., Bassilian, S., Lim, S., and Boros, L.G. (2000). Loss of regulation of lipogenesis in the Zucker diabetic (ZDF) rat. Am. J. Physiol. Endocrinol. Metab. *279*, E425–E432.

Lee, P.L., Jung, S.M., and Guertin, D.A. (2017). The complex roles of mechanistic target of rapamycin in adipocytes and beyond. Trends Endocrinol. Metab. *28*, 319–339.

Leroux, A.E., Schulze, J.O., and Biondi, R.M. (2018). AGC kinases, mechanisms of regulation and innovative drug development. Semin. Cancer Biol. *48*, 1–17.

Li, Y., Ma, Z., Jiang, S., Hu, W., Li, T., Di, S., Wang, D., and Yang, Y. (2017). A global perspective on FOXO1 in lipid metabolism and lipid-related diseases. Prog. Lipid Res. *66*, 42–49.

Manning, B.D., and Toker, A. (2017). AKT/PKB signaling: navigating the network. Cell *169*, 381–405.

Masui, K., Tanaka, K., Akhavan, D., Babic, I., Gini, B., Matsutani, T., Iwanami, A., Liu, F., Villa, G.R., Gu, Y., et al. (2013). mTOR complex 2 controls glycolytic metabolism in glioblastoma through FoxO acetylation and upregulation of c-Myc. Cell Metab. *18*, 726–739.

McCabe, B.J., Bederman, I.R., Croniger, C., Millward, C., Norment, C., and Previs, S.F. (2006). Reproducibility of gas chromatography-mass spectrometry measurements of 2H labeling of water: application for measuring body composition in mice. Anal. Biochem. *350*, 171–176.

Ménard, S.L., Croteau, E., Sarrhini, O., Gélinas, R., Brassard, P., Ouellet, R., Bentourkia, M., van Lier, J.E., Des Rosiers, C., Lecomte, R., and Carpentier, A.C. (2010). Abnormal in vivo myocardial energy substrate uptake in diet-induced type 2 diabetic cardiomyopathy in rats. Am. J. Physiol. Endocrinol. Metab. *298*, E1049–E1057.

Michishita, E., McCord, R.A., Boxer, L.D., Barber, M.F., Hong, T., Gozani, O., and Chua, K.F. (2009). Cell cycle-dependent deacetylation of telomeric histone H3 lysine K56 by human SIRT6. Cell Cycle *8*, 2664–2666.

Mihaylova, M.M., Vasquez, D.S., Ravnskjaer, K., Denechaud, P.D., Yu, R.T., Alvarez, J.G., Downes, M., Evans, R.M., Montminy, M., and Shaw, R.J. (2011). Class IIa histone deacetylases are hormone-activated regulators of FOXO and mammalian glucose homeostasis. Cell *145*, 607–621.

Mottillo, E.P., Balasubramanian, P., Lee, Y.H., Weng, C., Kershaw, E.E., and Granneman, J.G. (2014). Coupling of lipolysis and de novo lipogenesis in brown, beige, and white adipose tissues during chronic β3-adrenergic receptor activation. J. Lipid Res. *55*, 2276–2286.

Muzumdar, M.D., Tasic, B., Miyamichi, K., Li, L., and Luo, L. (2007). A global double-fluorescent Cre reporter mouse. Genesis *45*, 593–605.

Ortega-Molina, A., Efeyan, A., Lopez-Guadamillas, E., Muñoz-Martin, M., Gómez-López, G., Cañamero, M., Mulero, F., Pastor, J., Martinez, S., Romanos, E., et al. (2012). Pten positively regulates brown adipose function, energy expenditure, and longevity. Cell Metab. *15*, 382–394.

Pan, P.W., Feldman, J.L., Devries, M.K., Dong, A., Edwards, A.M., and Denu, J.M. (2011). Structure and biochemical functions of SIRT6. J. Biol. Chem. *286*, 14575–14587.

Peterson, T.R., Laplante, M., Thoreen, C.C., Sancak, Y., Kang, S.A., Kuehl, W.M., Gray, N.S., and Sabatini, D.M. (2009). DEPTOR is an mTOR inhibitor frequently overexpressed in multiple myeloma cells and required for their survival. Cell *137*, 873–886.

Pietrocola, F., Galluzzi, L., Bravo-San Pedro, J.M., Madeo, F., and Kroemer, G. (2015). Acetyl coenzyme A: a central metabolite and second messenger. Cell Metab. *21*, 805–821.

Roh, H.C., Tsai, L.T., Lyubetskaya, A., Tenen, D., Kumari, M., and Rosen, E.D. (2017). Simultaneous Transcriptional and epigenomic profiling from specific cell types within heterogeneous tissues in vivo. Cell Rep. *18*, 1048–1061.

Rosenwald, M., Perdikari, A., Rülicke, T., and Wolfrum, C. (2013). Bi-directional interconversion of brite and white adipocytes. Nat. Cell Biol. *15*, 659–667.

Rosner, M., and Hengstschläger, M. (2008). Cytoplasmic and nuclear distribution of the protein complexes mTORC1 and mTORC2: rapamycin triggers dephosphorylation and delocalization of the mTORC2 components rictor and sin1. Hum. Mol. Genet. *17*, 2934–2948.

Rothwell, N.J., and Stock, M.J. (1979). A role for brown adipose tissue in diet-induced thermogenesis. Nature *281*, 31–35.

Rowland, L.A., Maurya, S.K., Bal, N.C., Kozak, L., and Periasamy, M. (2016). Sarcolipin and uncoupling protein 1 play distinct roles in diet-induced thermogenesis and do not compensate for one another. Obesity (Silver Spring) *24*, 1430–1433.

Sanchez-Gurmaches, J., and Guertin, D.A. (2014). Adipocytes arise from multiple lineages that are heterogeneously and dynamically distributed. Nat. Commun. *5*, 4099.

Sanchez-Gurmaches, J., Hung, C.M., and Guertin, D.A. (2016). Emerging Complexities in Adipocyte Origins and Identity. Trends Cell Biol. *26*, 313–326.

Sanchez-Gurmaches, J., Tang, Y., Jespersen, N.Z., Wallace, M., Martinez Calejman, C., Gujja, S., Li, H., Edwards, Y.J.K., Wolfrum, C., Metallo, C.M., et al. (2018). Brown fat AKT2 is a cold-induced kinase that stimulates ChREBP-mediated de novo lipogenesis to optimize fuel storage and thermogenesis. Cell Metab. *27*, 195–209.e6.

Sarbassov, D.D., Guertin, D.A., Ali, S.M., and Sabatini, D.M. (2005). Phosphorylation and regulation of Akt/PKB by the rictor-mTOR complex. Science *307*, 1098–1101.

Saxton, R.A., and Sabatini, D.M. (2017). mTOR signaling in growth, metabolism, and disease. Cell *169*, 361–371.

Scheele, C., and Nielsen, S. (2017). Metabolic regulation and the anti-obesity perspectives of human brown fat. Redox Biol. *12*, 770–775.

Schrader, M., Costello, J., Godinho, L.F., and Islinger, M. (2015). Peroxisome-mitochondria interplay and disease. J. Inherit. Metab. Dis. *38*, 681–702.

Schreiber, R., Diwoky, C., Schoiswohl, G., Feiler, U., Wongsiriroj, N., Abdellatif, M., Kolb, D., Hoeks, J., Kershaw, E.E., Sedej, S., et al. (2017). Cold-induced thermogenesis depends on ATGL-mediated lipolysis in cardiac muscle, but not brown adipose tissue. Cell Metab. *26*, 753–763.e7.

Seale, P., Bjork, B., Yang, W., Kajimura, S., Chin, S., Kuang, S., Scimè, A., Devarakonda, S., Conroe, H.M., Erdjument-Bromage, H., et al. (2008). PRDM16 controls a brown fat/skeletal muscle switch. Nature *454*, 961–967.

Shiota, C., Woo, J.T., Lindner, J., Shelton, K.D., and Magnuson, M.A. (2006). Multiallelic disruption of the rictor gene in mice reveals that mTOR complex 2 is essential for fetal growth and viability. Dev. Cell *11*, 583–589.

Sidossis, L., and Kajimura, S. (2015). Brown and beige fat in humans: thermogenic adipocytes that control energy and glucose homeostasis. J. Clin. Invest. *125*, 478–486.

Tang, Y., Wallace, M., Sanchez-Gurmaches, J., Hsiao, W.Y., Li, H., Lee, P.L., Vernia, S., Metallo, C.M., and Guertin, D.A. (2016). Adipose tissue mTORC2 regulates ChREBP-driven de novo lipogenesis and hepatic glucose metabolism. Nat. Commun. *7*, 11365.

Thoreen, C.C., Kang, S.A., Chang, J.W., Liu, Q., Zhang, J., Gao, Y., Reichling, L.J., Sim, T., Sabatini, D.M., and Gray, N.S. (2009). An ATP-competitive mammalian target of rapamycin inhibitor reveals rapamycin-resistant functions of mTORC1. J. Biol. Chem. *284*, 8023–8032.

Trayhurn, P. (1981). Fatty acid synthesis in mouse brown adipose tissue. The influence of environmental temperature on the proportion of whole-body fatty acid synthesis in brown adipose tissue and the liver. Biochim. Biophys. Acta *664*, 549–560.

von Essen, G., Lindsund, E., Cannon, B., and Nedergaard, J. (2017). Adaptive facultative diet-induced thermogenesis in wild-type but not in UCP1-ablated mice. Am. J. Physiol. Endocrinol. Metab. *313*, E515–E527.

Wan, M., Easton, R.M., Gleason, C.E., Monks, B.R., Ueki, K., Kahn, C.R., and Birnbaum, M.J. (2012). Loss of Akt1 in mice increases energy expenditure and protects against diet-induced obesity. Mol. Cell. Biol. *32*, 96–106.

Yang, D., Diraison, F., Beylot, M., Brunengraber, D.Z., Samols, M.A., Anderson, V.E., and Brunengraber, H. (1998). Assay of low deuterium enrichment of water by isotopic exchange with [U-13C3]acetone and gas chromatography-mass spectrometry. Anal. Biochem. *258*, 315–321.

Yang, B., Zwaans, B.M., Eckersdorff, M., and Lombard, D.B. (2009). The sirtuin SIRT6 deacetylates H3 K56Ac in vivo to promote genomic stability. Cell Cycle *8*, 2662–2663.

Zechner, R., Zimmermann, R., Eichmann, T.O., Kohlwein, S.D., Haemmerle, G., Lass, A., and Madeo, F. (2012). FAT SIGNALS—lipases and lipolysis in lipid metabolism and signaling. Cell Metab. *15*, 279–291.

Zhong, L., D'Urso, A., Toiber, D., Sebastian, C., Henry, R.E., Vadysirisack, D.D., Guimaraes, A., Marinelli, B., Wikstrom, J.D., Nir, T., et al. (2010). The histone deacetylase Sirt6 regulates glucose homeostasis via Hif1alpha. Cell *140*, 280–293.

STAR★METHODS

KEY RESOURCES TABLE

REAGENT or RESOURCE	SOURCE	IDENTIFIER
Antibodies		
mTOR	Cell Signaling Technology	Cat# 2972;RRID: AB_330978
Raptor	Cell Signaling Technology	Cat# 2280;RRID: AB_561245
Rictor	Cell Signaling Technology	Cat# 2140;RRID: AB_561245
pan-AKT	Cell Signaling Technology	Cat# 9272;RRID: AB_329827
AKT1	Cell Signaling Technology	Cat# 2938;RRID: AB_915788
AKT2	Cell Signaling Technology	Cat# 3063;RRID: AB_2225186
NDRG1	Cell Signaling Technology	Cat# 9408;RRID: AB_11140640
ATGL	Cell Signaling Technology	Cat# 2439;RRID: AB_2167953
ACC	Cell Signaling Technology	Cat# 3676;RRID: AB_2219397
ACLY	Cell Signaling Technology	Cat# 4332;RRID: AB_2223744
FASN	Cell Signaling Technology	Cat# 3180;RRID: AB_2100796
HDAC4	Cell Signaling Technology	Cat# 7628;RRID: AB_10860255
HDAC5	Cell Signaling Technology	Cat# 20458;RRID: AB_2713973
HDAC7	Cell Signaling Technology	Cat# 33418;RRID: AB_2716756
HSL	Cell Signaling Technology	Cat# 4107;RRID: AB_2296900
SIRT1	Cell Signaling Technology	Cat# 9475;RRID: AB_2167130
SIRT3	Cell Signaling Technology	Cat# 5490;RRID: AB_10828246
SIRT6	Cell Signaling Technology	Cat# 12486;RRID: AB_2636969
FoxO1	Cell Signaling Technology	Cat# 2880;RRID: AB_2106495
PRAS40	Cell Signaling Technology	Cat# 2691;RRID: AB_2225033
α-Tubulin	Cell Signaling Technology	Cat# 2125;RRID: AB_2619646
Phospho-S473-AKT	Cell Signaling Technology	Cat# 4058;RRID: AB_331168
Phospho-T308-AKT	Cell Signaling Technology	Cat# 4056;RRID: AB_331163
Phospho-T450-AKT	Cell Signaling Technology	Cat# 9267;RRID: AB_823676
Phospho-S473-AKT1	Cell Signaling Technology	Cat# 9018;RRID: AB_2629283
Phospho-S474-AKT2	Cell Signaling Technology	Cat# 8599;RRID: AB_2630347
Phospho-T642-AS160	Cell Signaling Technology	Cat# 4288;RRID: AB_10545274
Phospho-T246-PRAS40	Cell Signaling Technology	Cat# 2997;RRID: AB_2258110
Phospho-T24-FoxO1	Cell Signaling Technology	Cat# 9464;RRID: AB_329842
Phospho-S256-FoxO1	Cell Signaling Technology	Cat# 9461;RRID: AB_329831
Phospho-T346-NDRG1	Cell Signaling Technology	Cat# 5482;RRID: AB_10693451
Phospho-HDAC4/5/7	Cell Signaling Technology	Cat# 3443;RRID: AB_2118723
Phospho-HDAC4/5/7	Cell Signaling Technology	Cat# 3424;RRID: AB_2118727
Phospho-S660-HSL	Cell Signaling Technology	Cat# 4126;RRID: AB_490997
Histon H3	Cell Signaling Technology	Cat# 4499;RRID: AB_10544537
Acetyl-Histone H3 (Lys9)	Cell Signaling Technology	Cat# 9649;RRID: AB_823528
Acetyl-Histone H3 (Lys56)	EMD Millipore	Cat# 07-990;RRID: AB_10806624
Acetylated-FOXO1	Santa Cruz biotechnology	Cat# sc-49437;RRID: AB_2247212
PPARγ	Santa Cruz biotechnology	Cat# sc-7273;RRID: AB_628115
UCP1	Abcam	Cat# ab10983;RRID: AB_2241462
Lamin B	Abcam	Cat# ab16048;RRID: AB_10107828
Phospho-S522-Perilipin1	Vala sciences	Cat# 4856;RRID: N/A

(*Continued on next page*)

Continued

REAGENT or RESOURCE	SOURCE	IDENTIFIER
FoxO1 (mouse monoclonal)	Cell Signaling Technology	Cat# 14952;RRID: AB_2722487
Chemicals, Peptides, and Recombinant Proteins		
$^{2}H_2O$	Sigma	151882
4-hydroxy Tamoxifen	Toronto research chemicals	H954729
Tamoxifen	Sigma	T5648
T3	Sigma	T2877
Insulin	Sigma	I2643
3-isobutyl-1-methylxanthine (IBMX)	Sigma	I5879
Dexamethasone	Sigma	D1756
Rosiglitazone	Cayman Chemical	71740
CL316,243	Tocris Bioscience	14-991-0
Isoproterenol	Sigma	I6504
Forskolin	Tocris Bioscience	10-991-0
AS1842856	Selleck Chemicals	S8222
Torin1	Tocris Bioscience	424710
GSK650394	Tocris Bioscience	890842-28-1
MK2202	Selleck Chemicals	S1078
LMK-235	Selleck Chemicals	S7569
[1-^{14}C]-2-bromopalmitic acid	Moravek	MC452
[1,2-^{3}H]-deoxy-D-glucose	Perkin Elmer	NET328A001MC
D-[U-^{14}C]-glucose	Perkin Elmer	NEC042V250UC
Free Glycerol Reagent	Sigma	F6428
Critical Commercial Assays		
High Capacity cDNA reverse transcription kit	Applied Biosystems	4368813
RNeasy kit	QIAGEN	74106
Direct cAMP ELISA kit	Enzo Life Sciences	ADI-900-066
Deposited Data		
Unprocessed scans of western blot data at Mendeley Data	This Study	https://doi.org/10.17632/jmhjb2p2x7.1
SIRT6 HaloTag affinity pull-down-MS primary data	This Study	See Table S1
Experimental Models: Cell Lines		
UBC-CreERT2;Rictor^{floxed} immortalized brown preadipocytes	This Study	N/A
UBC-CreERT2;Rictor^{floxed} immortalized white preadipocytes	This Study	N/A
Human embryonic kidney (HEK293)	ATCC	N/A
HeLa	ATCC	N/A
Experimental Models: Organisms/Strains		
Mouse: Rictor^{floxed}	Jackson labs	020649
Mouse: FoxO1^{floxed}	Jackson labs	024756
Mouse: FoxO1 ^{floxed} /Rictor^{floxed}	This Study	N/A
Mouse: UCP1-Cre	Jackson labs	024670
Mouse: Adiponectin-Cre	Jackson labs	010803
Mouse: UCP1-CreER	Christian Wolfrum lab	Rosenwald et al., 2013
Mouse: Akt1^{floxed}	Morrie Birnbaum lab	Wan et al., 2012
Mouse: Akt2^{floxed}	Morrie Birnbaum lab	Wan et al., 2012
Mouse: B6.129(Cg)-Gt(ROSA)26Sortm4(ACTB-tdTomato,-EGFP) Luo/J	Jackson labs	007676
Mouse: B6.Cg-Tg(UBC-cre/ERT2)1Ejb/2J	Jackson labs	008085

(*Continued on next page*)

Continued

REAGENT or RESOURCE	SOURCE	IDENTIFIER
Oligonucleotides		
Mouse primers	IDT	See Table S2
Recombinant DNA		
pLenti CRISPR V2 sgFoxO1_#1	This Study	See Table S2
pLenti CRISPR V2 sgFoxO1_#2	This Study	See Table S2
pLenti CRISPR V2 sgFoxO1_#3	This Study	See Table S2
pLenti CRISPR V2 sgFoxO1_#4	This Study	See Table S2
pLenti CRISPR V2 sgSIRT1_#1	This Study	See Table S2
pLenti CRISPR V2 sgSIRT1_#2	This Study	See Table S2
pLenti CRISPR V2 sgSIRT1_#3	This Study	See Table S2
pLenti CRISPR V2 sgSIRT3_#1	This Study	See Table S2
pLenti CRISPR V2 sgSIRT3_#2	This Study	See Table S2
pLenti CRISPR V2 sgSIRT3_#3	This Study	See Table S2
pLenti CRISPR V2 sgSIRT6_#1	This Study	See Table S2
pLenti CRISPR V2 sgSIRT6_#2	This Study	See Table S2
pLenti CRISPR V2 sgSIRT6_#3	This Study	See Table S2
pLenti CRISPR V2 sgHDAC4_#1	This Study	See Table S2
pLenti CRISPR V2 sgHDAC4_#3	This Study	See Table S2
pLenti CRISPR V2 sgHDAC5_#2	This Study	See Table S2
pLenti CRISPR V2 sgHDAC5_#3	This Study	See Table S2
pLenti CRISPR V2 sgHDAC7_#1	This Study	See Table S2
pLenti CRISPR V2 sgHDAC7_#2	This Study	See Table S2
pBabe-Puro-FoxO1_WT	This Study	N/A
pBabe-Puro-FoxO1_KR	This Study	N/A
pBabe-Puro-FoxO1_WT	This Study	N/A
Software and Algorithms		
Graphpad	GraphPad Software	https://www.graphpad.com/
Adobe Illustrator	Adobe	https://www.adobe.com/
FLIR Tools version 2.1	FLIR systems	https://www.flir.com/
ImageJ	Wayne Rasband	https://imagej.net/Welcome
Other		
Rodent incubators	Power Scientific	RIT33SD
Infrared thermal camera (FLIR T420)	FLIR	T420
Rectal thermometer probe	Braintree Scientific Inc.	Microtherma 2 system
High-fat diet (45% calories from fat)	ResearchDiet	Cat# D12451

LEAD CONTACT AND MATERIALS AVAILABILITY

Further information and request for resources and reagents should be directed to and will be fulfilled by the Lead Contact, David A. Guertin (david.guertin@umassmed.edu).

EXPERIMENTAL MODEL AND SUBJECT DETAILS

Mice

All mice used in this study were C57Bl6/J males. *Rictor*^{floxed} (Shiota et al., 2006), UCP1-Cre (JAX stock 024670), Adiponectin-Cre (JAX stock 010803), and *FoxO1*^{floxed} (JAX stock 024756) mice are available from Jackson laboratory. *Akt1*^{floxed} and *Akt2*^{floxed} mice are described in (Leavens et al., 2009; Wan et al., 2012). Ucp1-CreER is described in (Rosenwald et al., 2013). Floxed mouse strains were crossed with the different Cre-expressing mice to make tissue specific or inducible tissue specific knockout mice. Cre-negative floxed mice were used as controls. For studies using CreER mice, CreER only mice were included as an additional control.

Unless noted otherwise (e.g., in temperature studies), mice were housed in the UMMS Sherman Center Animal Medicine Facility in a clean room set at 22°C and 45% humidity on a daily 12h light/dark cycle, and kept in ventilated racks fed *ad libitum* with a standard chow diet, with bedding changed every two weeks. Mice were sacrificed at 7-30 weeks old depending on the experiment. Please see figure legend for specific age and number of mice used. All animal experiments were approved by the University of Massachusetts Medical School Institutional Animal Care and Use Committee.

Cell culture

Human embryonic kidney (HEK293) and HeLa cell lines were from American Type Culture Collection (ATCC). For *Rictor-iKO* cell lines, primary brown preadipocytes were isolated from *Ubc-CreERT2;Rictor* ^{floxed} neonates at postnatal day 1 and immortalized with pBabe-SV40 Large T according to a standard protocol (Fasshauer et al., 2001) as described in (Hung et al., 2014). The gender of each neonate was not determined. Cells were maintained in high-glucose (25 mM) DMEM in incubators at 37°C and 5% CO_2. Cells stably expressing recombinant proteins were obtained using a retroviral system. For primary, non-immortalized cells (i.e., from *Adiponectin-Cre;Rictor* and *Adiponectin-Cre;FoxO1* mice), the immortalization step was excluded.

METHOD DETAILS

Thermogenic (brown, brite/beige) adipocyte differentiation

For brown adipocyte differentiation, cells were seeded (Day-1) at medium density and allowed to proliferate to confluence in the presence of high-glucose DMEM including 10% FBS, 1% antibiotics, 20 nM insulin and 1 nM T3. After 3 days (Day-4), cells were induced to differentiate by adding induction media (high-glucose DMEM including 10% FBS, 1% antibiotics, 20 nM insulin, 1 nM T3, 0.125 mM indomethacin, 2 μg/mL dexamethasone and 0.5 mM 3-isobutyl-1-methylxanthine (IBMX)) for 2 days. After this, the medium (high-glucose DMEM including 10% FBS and 1% antibiotics) with insulin and T3 was changed every 2 days until Day-11. *Rictor* deletion was achieved by treating the cells with 4-hydroxytamoxifen (1 μM 4-OHT) on Day-6 of differentiation, which by-passes the requirement for Rictor in PPAR-γ induction (Hung et al., 2014). Control cells received an equivalent volume of ethanol, the vehicle used to dissolve 4-OHT. To stimulate β-adrenergic signaling, CL-316,243 (0.1-1 μM), isoproterenol (1-10 μM), or forskolin (1-10 μM), was administered directly to cells in culture that had been given fresh medium (high-glucose DMEM including 10% FBS, 1% antibiotics, 20 nM insulin and 1 nM T3) 24-hours before treatment.

For brite/beige cell analysis, white preadipocytes were from the subcutaneous vascular fraction (SVF) of *Ubc-CreERT2;Rictor*^{floxed} mice in 6-8 weeks of age. SVF were isolated by digesting the inguinal WAT in digestion buffer (123 mM NaCl, 5 mM KCl, 1.3 mM $CaCl_2$, 5 mM glucose, 100 mM HEPES, 1% antibiotics and 4% BSA at pH 7.4 containing 1.5 mg/mL of collagenase A). The isolated cells were immortalized by a 3T3 immortalization protocol as previously described (Tang et al., 2016). Cells were maintained in 25 mM glucose, pyruvate-containing DMEM in incubators at 37°C and 5% CO_2. For brite/beige adipocyte differentiation, cells were seeded at medium density and allowed to proliferate to confluence in the presence of high-glucose DMEM including 10% FBS, 1% antibiotics (complete medium). Two days after they reached confluency, cells were induced to differentiate by adding induction media (high-glucose DMEM including 10% FBS, 1% antibiotics, 100 nM insulin, 2 μg/mL dexamethasone, 0.5mM 3-isobutyl-1-methylxanthine (IBMX), 1 nM Rosiglitazone and 1 nM T3) for 4 days (Day 1 to 5) and replaced with medium containing 100 nM insulin and T3. Then the complete medium was changed every 2 days until day 9. *Rictor* deletion was achieved by treating the cells with 4-hydroxytamoxifen (4-OHT, 1 μM), equivalent volume of ethanol for control, on Day-5 of differentiation. To stimulate β-adrenergic signaling, forskolin (10 mM), was administered directly to cells in culture that had been given fresh medium (high-glucose DMEM including 10% FBS, 1% antibiotics, 100 nM insulin and 1 nM T3) 24-hours before treatment.

Fasting/Refeeding

Mice were fasted overnight, then refed by adding food to their cages for 1 hour before dissection.

Tissue Histology

Tissue pieces were fixed in 10% formalin. Embedding, sectioning and Hematoxylin and Eosin (H&E) staining was done by the UMMS Morphological Core facility. Oil red O staining was applied on liver cryo-sections by the UMMS Morphological Core facility.

Whole Mount Confocal Microscopy

Small pieces of adipose tissues were mounted with Fluoromount-G (Southern Biotech) and imaged on a LSM 5 Pascal (Zeiss) point scanner confocal system using a 10x or 40x oil immersion objective. eGFP was excited at 488 nm and detected from 515 to 565 nm. tdTomato (red fluorescent protein) was excited at 543 nm and detected from 575 to 640 nm.

Cold challenge experiments

For acute cold challenge, 10-week old *Ucp1-Cre;Rictor*^{Floxed} and littermate control mice were transferred early in the morning to pre-chilled cages in a 4°C cold room with free access to pre-chilled food and water. Rectal temperature was measured hourly using a rectal probe (RET-3, ThermoWorks). For chronic cold challenge, the animals were placed in a 6°C thermal chamber (Model RIT330SD Power Scientific) for two weeks with free access to food and water, and maintained on the standard day/night light cycle. BAT and tail

temperatures were obtained using an infrared thermal camera (FLIR T420) in lightly anesthetized mice and analyzed with FLIR tools.

Diet challenge experiments

6-week-old *Ucp1-Cre;Rictor*^{Floxed} mice and littermate control mice were transferred to a thermoneutral chamber (30°C) with a standard day/night light cycle and maintained on a standard chow diet (Prolab Isopro RMH3000, LabDiet). At 10-weeks of age, mice were either kept on the chow diet, or switched to a high-fat diet (45% calories from fat; ResearchDiet # D12451). Body weight and food intake were accessed weekly for 16 weeks. For experiments with the *Ucp1-CreER;Rictor*^{Floxed} mice, all mice in both the control and experimental groups were injected (I.P.)with Tamoxifen (100 mg/kg per day) at 20-weeks of age for 6 consecutive days. After tamoxifen treatment, the mice were transferred into a thermoneutral chamber (30°C) for one-week adaptation, then either kept on chow diet or switched to 45% HFD. Total body weight and food intake was monitored weekly. Tamoxifen was dissolved in corn oil/ethanol (9:1 vol/vol) at 2 mg/mL by shaking at 4°C overnight. 6-week-old *Ucp1-CreERT2;Akt1*^{Floxed} mice, *Ucp1-CreERT2;Akt2*^{Floxed} mice and respective littermate control mice were injected with tamoxifen (20 mg/mL, at 2 mg/day/mouse 5 times in a period of seven days. At 9-weeks old, mice were transferred to a thermoneutral chamber (30°C) with a standard day/night light cycle and maintained on a standard chow diet (Prolab Isopro RMH3000, LabDiet). At 10-weeks of age, mice were either kept on the chow diet or switched to a high-fat diet (45% calories from fat; ResearchDiet # D12451).

Glucose tolerance test (GTT) and blood metabolite analysis

Overnight fasted animals were subjected to GTT by intraperitoneally injecting glucose at 2 g/kg of body weight, and blood glucose levels were measured by tail bleeding with a commercially available glucose meter. The analysis of blood metabolites was performed by the MMPC at the University of Cincinnati.

Lipolysis assays

Standard ex-vivo lipolysis assays were performed as described in (Schreiber et al., 2017). Briefly, fresh dissected interscapular BAT was put into high-glucose DMEM supplemented with 2% fatty acid (FA)-free BSA. The tissue was minced into small pieces and pre-incubated with DMEM containing 2% FA-free BSA in 96-well plates for 30 minutes. To analyze basal lipolysis, the tissue pieces were transferred into 150 μL of fresh media and incubated for 1 hr in a tissue culture incubator. To analyze agonist-stimulated lipolysis, tissues were pre-incubated in 150 μL DMEM containing 2% fatty acid (FA)-free BSA with isoproterenol (ISO, 10 μM) for 30 min then transferred into the same medium for an additional 2 hr. To determine the amount of basal and stimulated lipolysis, the glycerol content of the medium was analyzed using free glycerol reagent (F6428, Sigma). Protein quantifications of each tissue sample were determined by Bradford assay (Bio-rad, #5000006), and the total amount of lipolysis was calculated as nmol of glycerol per mg/protein. For *in vitro* lipolysis assay, the same experimental procedure was performed using the cultured brown adipocytes.

Glucose and fatty acid uptake assays

^{14}C-bromopalmitate ([1-^{14}C]-2-bromopalmitic acid) and ^{3}H-deoxyglucose ([1,2-3H(N)]-Deoxy-D-glucose) were used to evaluate NEFA and glucose uptake respectively into BAT, VAT, muscle and liver as previously described in (Ménard et al., 2010; Labbé et al., 2016). Both radioactive tracers (Moravek Biochemicals, Inc. Brea, CA, USA) were dissolved in normal saline supplemented with 4% bovine serum albumin (BSA). Following a 6-hr fast, the mice received an intraperitoneal bolus of 10 μCi of each tracer in a total volume of 150 μl. Two hours following the injection, mice were euthanized with an overdose of anesthetic, and tissue samples were collected, weighed and homogenized. Specific fractional uptakes of ^{14}C-bromopalmitate and ^{3}H-deoxyglucose were determined using a scintillation counter (liquid scintillation analyzer Tri-Carb 2900TR, PerkinElmer, Montreal, QC, Canada). Nutrient uptake data is expressed as the percentage of injected dose of [^{14}C] and [^{3}H] per milligram of tissue.

Cellular cAMP measurement assay

Using differentiated brown adipocytes, cellular cAMP level was measured following the instructions of the direct cAMP ELISA Assay kit (Enzo Life Sciences, Inc., Exeter, UK).

Immunofluorescence assay

Cells growing on coverslips in 6-cm dishes were fixed with 4% paraformaldehyde at room temperature for 15 min, followed by blocking with 5% BSA in PBS for 30 min, and then incubation with primary FoxO1 antibody (1:100) at 4°C overnight. After washing with PBS five times, the coverslips were stained with secondary antibodies (AlexaFluor-488-conjugated goat anti-rabbit IgG, Invitrogen, 1:400) at room temperature for 2 hours. Coverslips were also stained with DAPI (Sigma) and mounted on glass slides. Cells were examined with a laser-scanning confocal microscope (Leica).

Subcellular fractionation assay

The Subcellular Protein Fractionation Kit for Cultured Cells (Thermo-Scientific, cat. no. 78840) was used for subcellular fractionations following the manufacturer's protocol.

Construction of small guide RNAs, lentiviral infection and retroviral infection

Gene-specific custom designed single guide RNAs were cloned into the lentiCRISPRv2 vector (Addgene). The sgRNA sequence was determined by the CRISPR Design Tool (http://chopchop.rc.fas.harvard.edu/) and sequences for sgRNAs targeting the FoxO1, SIRT1, SIRT3, SIRT6, HDAC4, HDAC5 and HDAC7 genes are shown in Table S2. To generate lentiviruses, HEK293T cells were transfected with lentiviral vectors expressing the sgRNA of interest in combination with VSV-G envelope plasmid and Delta-Vpr packing plasmid. To generate retroviruses, HEK293T cells were transfected with pBABE-retroviral vectors expressing FoxO1, FoxO1-6KR, and FoxO1-6KQ in combination with the retroviral packaging DNA (pEco), respectively. Culture media was changed 12 hours after transfection and the virus-containing supernatant was collected 48 hours after transfection and passed through a 0.45 μm filter to remove host cells. Brown preadipocytes were infected in medium containing 4 μg/mL of polybrene (Sigma) by centrifugation at 1800 RPM for 30 min. 24 hours after the infection, cells were trypsinized and subjected to antibiotic selection.

Western blot analysis and immunoprecipitation assays

Cells were harvested in cold PBS and lysed in protein lysis buffer (1% Triton X-100, 50 mM HEPES at pH 7.4, 150 mM NaCl, 10mM β-glycerophosphate, 2 mM EDTA, protease/phosphatase inhibitor cocktail). For immunoblot analysis of surgically dissected fat tissue depots, tissues were homogenized and lysed in RIPA buffer (150 mM NaCl, 50 mM HEPES at pH 7.4, 0.1% SDS, 1% Triton X-100, 2 mM EDTA, 0.5% Na-deoxycholate) containing a protease and phosphatase inhibitor cocktail. Protein lysates were mixed with 5X SDS sample buffer and boiled, separated by SDS-PAGE, transferred to polyvinylidene difluoride (PVDF) membrane filters and subjected to immunoblot analysis. For immunoprecipitationfor mTOR complex and SIRT6, cells were lysed in ice-cold mTOR IP buffer (0.3% CHAPS, 40 mM HEPES at pH 7.4, 150 mM NaCl, 5% glycerol, 2 mM EDTA, and protease/phosphatase inhibitor cocktail). 0.5∼2mg of cell lysates were incubated with the appropriate primary antibodies (for 12-16 hr), then with protein G agarose beads (Invitrogen) at 4°C for 2 h. Immuno-complexes were centrifuged, and washed twice with lysis buffer, then eluted from the beads by adding 2X SDS sample buffer and boiling. Immunoblot analysis was subsequently performed using the indicated antibodies.

FoxO1 acetylation assays

To detect endogenous acetylated FoxO1, cells were lysed in protein lysis buffer containing 10 mM Nicotinamide (NAM), 5 μM TSA 0.2% SDS. 0.5∼1mg of cell lysates were combined with anti-Acetyl Lysine (CST #9441) antibody and then incubated overnight with gentle rotation. On the next day, 20 μl of protein G agarose beads were added and incubated for an additional 2 hr. Beads were washed three times using lysis buffer, and the precipitates were eluted in 2X sample buffer and boiled. The acetylated-FoxO1 proteins were detected by immunoblotting using the anti-FoxO1 total protein antibody. The acetylated-FoxO1 protein was also detected in protein lysates using an acetylation-specific FoxO1 (sc-49437) antibody.

Gene expression analysis

Total RNA was isolated from cells or tissues using Qiazol (QIAGEN) and an RNeasy kit (QIAGEN). Equal amounts of RNA were retrotranscribed to cDNA using a High capacity cDNA reverse transcription kit (#4368813, Applied Biosystems). Quantitative RT-PCR (qRT-PCR) was performed in 10 μL reactions using a StepOnePlus real-time PCR machine from Applied Biosystems using SYBR Green PCR master mix (#4309156, Applied Biosystems) according to manufacturer instructions. Standard and melting curves were run in every plate for every gene to ensure efficiency and specificity of the reaction. TATA-box binding protein (Tbp) gene expression was used as a normalization gene in all conventional RT-PCR experiments. Data analysis was performed on web-based software provided by the manufacturer. Primer sequences are shown in Table S2

In vivo measurement of *de novo* synthesized fatty acid

^2H_2O method 3-days prior to termination, mice were I.P injected with 0.035 ml/g body weight 0.9% NaCL ^2H_2O, and drinking water was replaced with 8% ^2H_2O enriched water. Mice were fasted for 6 hours prior to plasma and tissue collection.

Plasma ^2H_2O enrichment

The ^2H labeling of water from samples or standards was determined via deuterium acetone exchange (McCabe et al., 2006; Yang et al., 1998). 5 μL of sample or standard was reacted with 4 μL of 10N NaOH and 4 μL of a 5% (v/v) solution of acetone in acetonitrile for 24 hours. Acetone was extracted by the addition of 600 μL chloroform and 0.5 g Na_2SO_4 followed by vigorous mixing. 100 μL of the chloroform was then transferred to a GCMS vial. Acetone was measured using an Agilent DB-35MS column (30 m 3 0.25mm i.d. 3 0.25 mm, Agilent J&W Scientific) installed in an Agilent 7890A gas chromatograph (GC) interfaced with an Agilent 5975C mass spectrometer (MS) with the following temperature program: 60°C initial, increase by 20°C/min to 100°C, increased by 50°C/min to 220°C, and held for 1 min. The split ratio was 40:1 with a helium flow of 1 ml/min. Acetone eluted at approximately 1.5 min. The mass spectrometer was operated in the electron impact mode (70 eV). The mass ions 58 and 59 were integrated and the % M1 (m/z 59) calculated. Known standards were used to generate a standard curve and plasma % enrichment was determined from this. All samples

were analyzed in triplicate. Total fatty acids were extracted from tissues and plasma using a bligh and dyer based methanol/chloroform/water extraction with C16 D31 as an internal standard. Briefly, 500 μls MeOH, 500 μls $CHCl_3$, 200 μL H_2O and fatty acid isotope internal standards were added to weighed pre-ground tissue. This was vortexed for 10 minutes followed by centrifugation at 10,000 g for 5 minutes. The lower chloroform phase was dried and then derivatized to form fatty acid methyl esters via addition of 500 μls 2% H_2SO_4 and incubation at 50°C for 2 hours. FAMES were extracted via addition of 100 μL saturated salt solution and 500 μL hexane, and these were analyzed using a Select FAME column (100 m x 0.25mm i.d.) installed in an Agilent 7890A GC interfaced with an Agilent 5975C MS using the following temperature program: 80°C initial, increase by 20°C/min to 170°C, increased by 1°C/min to 204°C, then 20°C/min to 250°C and held for 10 min.

Calculations

The % mass isotopomer distributions of each fatty acid was determined and corrected for natural abundance using in-house algorithms adapted from Fernandez et al., (Fernandez et al., 1996). Calculation of the fraction of newly synthesized fatty acids (FNS) was based on the method described by Lee et al., (Lee et al., 2000) where FNS is described by the following equation:

$$FNS = ME/(n \times p)$$

Where ME is the average number of deuterium atoms incorporated per molecule (ME = 1 x m1 + 2 x m2 +3 x m3 …), p is the deuterium enrichment in water and n is the maximum number of hydrogen atoms from water incorporated per molecule. N was determined using the equation:

$$m2/m1 = (N\text{-}1)/2\ xp/q$$

As described by Lee et al., (Lee et al., 1994) where q is the fraction of hydrogen atoms and p + q = 1. The molar amount of newly synthesized fatty acids was determined by:

$$MNS = FNS \times \text{total fatty acid amount}\ (\text{nmoles/mg tissue})$$

In vitro measurement of *de novo* synthesized fatty acid

Cells were incubated for 3 days with DMEM in which 0.01% of the total glucose concentration of the medium was comprised of D-[U-^{14}C]-glucose. Chloroform extraction was performed and labeled lipids were measured using a scintillation counter. Each sample was normalized to total protein concentration (Deberardinis et al., 2006)

HaloTag Mammalian Pull-Down Assay

N-terminal HaloTag fusions of human full-length SIRT6 (Q8N6T7) was obtained from Kazusa DNA Research Institute (Kisarazu, Japan) as a pFN21A vector (Promega). HaloTag control vector (Promega G6591) was used for expression of the HaloTag protein alone. HEK293T cells (10×10^6) or HeLa cells (12×10^6) were plated and grown overnight to 70%–80% confluency. HaloTag-SIRT6 (Experimental) or HaloTag alone (Control) vectors were then transfected using FuGENE HD Transfection Reagent (Promega) according to manufacturer's protocol. Cells expressing HaloTag-SIRT6 or HT-Ctrl were harvested and lysed on ice with 50mM Tris-HCl, pH 7.5, 150mM NaCl, 1% Triton X-100, and 0.1% sodium deoxycholate supplemented with Protease Inhibitor cocktail (Promega) and RQ1 RNase-Free DNase (Promega). Lysate was then homogenized with a syringe and centrifuged at 14.000 x g for 5 min. Experimental and control lysates were then incubated with HaloLink Resin (Promega) that had been pre-equilibrated in resin wash buffer (TBS and 0.05% IGEPAL CA-640 (Sigma)) for 15 min at 22°C with rotation to capture HaloTag-SIRT6 and any interacting protein partners. Resin was then washed 5 times with TBS wash buffer and protein interactors were eluted with SDS elution buffer (50mM Tris-HCl, pH 7.5, and 1% SDS).

MASS SPECTROMETRY ANALYSIS

HaloTag pulldown purified complexes from both HEK293 and HeLa samples were analyzed and processed by MS Bioworks, LLC (Ann Arbor, Michigan). Elution samples were pulsed onto an SDS-PAGE gel and cut into 10 slices. Each gel slice was washed using 25 mM ammonium bicarbonate and acetonitrile, followed by reduction with 10 mM dithiothreitol, and alkylation with 50 mM iodoacetamide. Proteins from each slice treated for 4hr with trypsin (Promega) and quenched with formic acid. Digests were then analyzed by nano LC/MS/MS with a NanoAcquity HPLC (Waters) interfaced with an Orbitrap Velos Pro (Thermo Scientific) tandem mass spectrometer. Resulting data were searched with Mascot (Matrix Science) against the concatenated forward/decoy UniProt Human Database, and Mascot DAT files were visualized and filtered by Scaffold (Proteome Software). Data were filtered using a minimum protein value of 90%, a minimum peptide value of 50% (Protein and Peptide Prophet scores), requiring at least two unique peptides per protein. Spectral counting was performed and normalized spectral abundance factors determined. Data were reported at less than 1% false discovery rate (FDR) at the protein level based on counting the number of forward and decoy matches.

QUANTIFICATION AND STATISTICAL ANALYSIS

Data are presented as mean + SEM, unless stated otherwise. Student's t test, non-parametric Mann-Whitney test or analysis of variance (ANOVA; one or two ways), as appropriate, were used to determine statistical significance. Statistical analysis was done using GraphPad Prism. The number of mice used per experiment is stated in each figure legend.

DATA AND CODE AVAILABILITY

Original, unprocessed data from this manuscript have been deposited to Mendeley Data at: https://doi.org/10.17632/jmhjb2p2x7.1